The Astronomical Journal, 156:27 (19pp), 2018 July https://doi.org/10.3847/1538-3881/aac5de


# Masses and Radii of Four Very Low-mass Stars in F+M Eclipsing Binary Systems

Priyanka Chaturvedi[1,2], Rishikesh Sharma[1], Abhijit Chakraborty[1], B. G. Anandarao[1], and Neelam J. S. S. V Prasad[1]
[1] Astronomy & Astrophysics Division, Physical Research Laboratory, Ahmedabad 380009, India; priyanka.chaturvedi@tifr.res.in
[2] Department of Astronomy & Astrophysics, Tata Institute of Fundamental Research, Homi Bhabha Road, Mumbai 400 005, India
*Received 2018 March 1; revised 2018 May 8; accepted 2018 May 14; published 2018 June 28*

## Abstract

Eclipsing binaries (EBs) with one of the companions as very low-mass stars (VLMSs; or M dwarfs) are testbeds to substantiate stellar models and evolutionary theories. Here we present four EB candidates with F-type primaries, namely, SAO 106989, HD 24465, EPIC 211682657, and HD 205403, identified from different photometry missions, SuperWASP, Kilodegree Extremely Little Telescope (KELT), *Kepler 2* (*K2*), and *Solar Terrestrial Relations Observatory* (*STEREO*). Using the high-resolution spectrograph PRL Advanced Radial velocity Abu-sky Search at the 1.2 m telescope at Mount Abu, Rajasthan, India, we hereby report the detection of four VLMSs as companions to the four EBs. We performed spectroscopic analysis and found the companion masses to be $0.256 \pm 0.005$, $0.233 \pm 0.002$, $0.599 \pm 0.017$, and $0.406 \pm 0.005\,M_{\odot}$ for SAO 106989, HD 24465, EPIC 211682657, and SAO 106989B, respectively. We determined orbital periods of $4.39790 \pm 0.00001$, $7.19635 \pm 0.00002$, $3.142023 \pm 0.000003$, and $2.444949 \pm 0.000001$ days and eccentricities of $0.248 \pm 0.005$, $0.208 \pm 0.002$, $0.0097 \pm 0.0008$, and $0.002 \pm 0.002$ for EBs SAO 106989, HD 24465, EPIC 211682657, and HD 205403, respectively. The radii derived by modeling the photometry data are $0.326 \pm 0.012\,R_{\odot}$ for SAO 106989, $0.244 \pm 0.001\,R_{\odot}$ for HD 24465B, $0.566 \pm 0.005\,R_{\odot}$ for EPIC 211682657B, and $0.444 \pm 0.014\,R_{\odot}$ for HD 205403B. The radii of HD 24465B and EPIC 211682657B have been measured by precise *Kepler* photometry and are consistent with theory within the error bars. However, the radii of SAO 106989B and HD 205403B, measured by KELT and *STEREO* photometry, are 17%–20% higher than those predicted by theory. A brief comparison of the results of the current work is made with the M dwarfs already studied in the literature.

*Key words:* stars: individual (SAO 106989, HD 24465, EPIC 211682657, HD 205403) – stars: low-mass – techniques: radial velocities

## 1. Introduction

Studies based on the nature of stellar initial mass function (IMF) have indicated that very low-mass stars (VLMSs) with masses $\leqslant 0.6\,M_{\odot}$ are the most ubiquitous objects created during star formation. The IMF was determined for the first time to be a power-law function that decreases with stellar masses in the mass range of 1–10 $M_{\odot}$ (Salpeter 1955). Recent work in this field has suggested that the stellar IMF breaks from a power-law form at 0.5 $M_{\odot}$ with a broad peak between 0.1 and 0.5 $M_{\odot}$ and falling at either side of this mass range (Luhman et al. 2000; Luhman 2000; Kroupa 2002; Chabrier 2003; Lada 2006). Thus, VLMSs form $\sim$70% of the total stellar systems within a distance of 10 pc (Henry et al. 2006). With the advent of large infrared arrays, there have been many successful attempts to survey through large-field imaging of VLMS objects by many space-based surveys, such as the *Spitzer Space Telescope* mission (Werner et al. 2004), *Herschel* (Pilbratt et al. 2010), and the *Wide-field Infrared Survey Explorer* (*WISE*; Wright et al. 2010). These surveys have led to identification and characterization of several VLMS objects (Luhman et al. 2012; Gagné et al. 2014; Bardalez Gagliuffi et al. 2015; Gillon et al. 2017; Suárez et al. 2017; Theissen et al. 2017). Some of the ground-based surveys, such as the Sloan Digital Sky Survey (SDSS; York et al. 2000), Two Micron All Sky Survey (2MASS; Skrutskie et al. 2006), and the Visible and Infrared Survey Telescope for Astronomy (VISTA; Emerson 2001), also have contributed similarly to the detection of VLMSs. However, there have been limited studies on the accurate determination of masses, radii, and other physical properties of VLMSs due to their intrinsic low-luminosity nature.

Testing of various stellar structural and evolutionary models involves precise measurements of physical parameters such as age, mass, radius, temperature, and chemical composition of the stars (Torres et al. 2010). Accurate determination of such stellar parameters is possible by studying eclipsing binaries (EBs) by methods such as astrometry, radial velocity (RV), and transit photometry. Such techniques of RV and transit photometry have been applied to hundreds of EBs studied in the literature (Andersen 1991; Torres et al. 2010 and references therein). A vast majority of observations of M dwarfs for varying masses have reported a higher radius by 10%–20% and a lower temperature by 5%–10% than those predicted by the models (Chabrier & Baraffe 2000; Torres & Ribas 2002; Ribas 2003; López-Morales & Ribas 2005; López-Morales 2007; Ribas et al. 2008; Torres et al. 2014; Baraffe et al. 2015; Lubin et al. 2017). In particular, the mid-M dwarfs (M3) that form the boundary between stars having radiative zones and those with totally convective zones (Chabrier & Baraffe 2000) are reported to show the most glaring discrepancies in the measurement of radii when compared with the theoretical models (López-Morales 2007). The mismatch of the radii as seen in these stars is termed the "M-dwarf radius problem" (Triaud et al. 2013).

A stellar activity hypothesis suggests that the aforementioned disagreement between theory and observations may be primarily caused by the degree of magnetic activity in stars: strong magnetic fields inhibit convection, leading to inflated stellar radii (Mullan & MacDonald 2001; López-Morales &

Ribas 2005; Torres 2013). López-Morales & Ribas (2005) proposed a scenario based on energy conservation mechanisms in star spot–covered areas. The dynamo-generated magnetic fields affect the convectional stability criteria for the stars, leading to a bloated radius at the same temperature or lower temperatures for the same radius. There is an inherent assumption that strong magnetic field regions and star spots are cooler than their surroundings. Thus, the suppressed photospheric temperatures lead to measured inflated stellar radii in order to maintain the radiative equilibrium and hydrostatic equilibrium. Chabrier et al. (2007) concluded in their study that the inhibition of convection in fast-rotating stars and the presence of star spots on the stellar disk could affect the stellar models. Current atmospheric models are not accurate due to some missing opacity components, leading to larger radii for stars having higher metallicity. Berger et al. (2006) found in their study that the disagreement is larger among metal-rich stars than metal-poor stars. This hypothesis suggests the dependency of metallicity on the amount of inflation for the measured radius.

Double-lined EBs—specifically, M-M EBs having masses and radii determined at high accuracies (~2%), like CM Dra (Morales et al. 2009), Cu CnC (Ribas 2003), YY Gem (Torres & Ribas 2002), and Gu Boo (López-Morales & Ribas 2005)—are paradigms used to test observations against theoretical models. The fundamental parameters of M dwarfs have been determined by a variety of methods, including spectral energy distribution, a combination of photometric and spectroscopic parameters, and similar such methods. Comparing the best-studied M dwarfs in EBs with the theoretical models using a range of isochrones of different ages and metallicities has seemed to reduce the scatter seen in the mass–radius diagram of M dwarfs (Torres 2013). In order to further reduce the scatter, there is a need to have stellar parameters derived with high accuracy and precision for a range of systems by different methods. Single-lined detached EB systems where VLMS objects occur as companions to brighter F-, G-, and K-type stars provide a huge sample to fill the gap from observations. The RV and transit photometry techniques ensure indirect determination of stellar parameters at high accuracies. The RV technique applied to F-, G-, and K-type primaries helps determine the projected mass of the companion, whereas photometry of these targets gives insights on the angle of orbital inclination and radii of both of the components, providing us a complete picture of the EB system. The F-type primaries accompanied by M-type secondaries (hereafter F+M binaries) in EBs are very often discovered in photometric surveys, as they have a resemblance to hot Jupiters transiting main-sequence stars (e.g., Bouchy et al. 2005; Beatty et al. 2007). However, only a handful of F+M EBs have been studied for their masses, radii, and orbital parameters (e.g., Pont et al. 2005a, 2005b, 2006; Fernandez et al. 2009; Chaturvedi et al. 2014). Statistically, there is a higher probability of finding M dwarfs as companions of F-type primaries than of finding equal-mass binary pairs (Bouchy et al. 2011a, 2011b; Moe & Di Stefano 2015). In order to understand the binarity fraction for F- and M-type stars, every additional system discovered and analyzed plays a key role in making the sample of F+M binaries larger and thereby an important subset of stellar studies. Duquennoy & Mayor (1991) found a 57% binarity fraction for late F- and G-type stars for a distance-limited sample within 22 pc of the Sun. Similar studies of F-type stars ($1.1\,M_\odot \geqslant M \leqslant 1.7\,M_\odot$) by Fuhrmann et al. (2012) and Fuhrmann & Chini (2015) found that the majority of F-type stars (~2/3 of them) are multiple by nature. The F-type stars have a range of rotational velocities (Nordström et al. 2004), and the exteriors of these stars range from having convective envelopes (late F-type stars) to radiative envelopes (mid-to-early F-type stars). Stars more massive than F type (O, B, and A type) are difficult to study for their binarity because of their high stellar rotation rates and relatively smaller sample size. The higher temperatures lead to less photospheric lines in the spectra. Moreover, these lines are rotationally broadened, thereby decreasing the quality of the stellar spectra and spectroscopic precision. Many of the early-type stars have stellar pulsations, making detection of companions very difficult. There have been only handful of such detections, for example, the case of WASP-33b (Herrero et al. 2011 and references therein). Thus, F-type stars occurring in binary pairs will be valuable contributions for understanding the multiplicity fraction of early-type stars.

We have initiated the EB program by the PRL Advanced Radial velocity Abu-sky Search (PARAS; Chakraborty et al. 2014) with a motivation to study single-lined detached EBs having potential M-dwarf companions. We have previously reported the detection and characterization of two EBs with PARAS, a 0.286 $M_\odot$ M dwarf across an F-type primary (Chaturvedi et al. 2014) and a 0.098 $M_\odot$ late-type M dwarf across a K-type primary (Chaturvedi et al. 2016). In this third paper of the series, we present spectroscopic and photometric investigations of four F-type sources: SAO 106989, HD 24465, EPIC 211682657, and HD 205403. All of these stars are EBs of short orbital period with putative M dwarfs in orbit. This study is intended to determine the masses, radii, and orbital parameters of the four putative M dwarfs. We describe the program stars briefly in Section 2. This is followed by a description of the RV observations of the stars in Section 3. We also discuss the high-resolution spectroscopic and photometric methods of analysis used to derive the physical parameters concerning all of the EBs in this section. In Section 4, we discuss the importance of this work, followed by a brief summary in Section 5.

## 2. Program Stars and Observations

Selection of EB candidates involved choosing stars brighter than ~11 in the $V$ band, as it is the faintest limit for PARAS with the 1.2 m telescope. Spectral types from F to K were chosen, as these stars have more spectral lines for precise RV measurements. Candidates were also chosen based on the coordinates in the non-monsoon months between October and May of the observing season at Mt. Abu. The current interest being VLMS candidates having an upper cutoff for the transit depth at ~50 mmag have been chosen in order to avoid samples having massive secondaries as companions. The lower-limit cutoff of the transit depth while short-listing candidates is kept at ~12 mmag to avoid planetary candidates. Based on these selection criteria, nearly a dozen targets have been short-listed from a list of a few hundred EB candidates picked from various photometric surveys like the *Solar Terrestrial Relations Observatory* (*STEREO*; Wraight et al. 2012), SuperWASP (SW; Christian et al. 2006; Clarkson et al. 2007; Lister et al. 2007; Street et al. 2007; Kane et al. 2008), and *Kepler* (Barros et al. 2016).

*STEREO* consists of two spacecraft (*A* and *B*) primarily dedicated to looking at the Sun and its environment. The Heliospheric Imager (HI-1) on the ahead spacecraft (HI-1A) has been used to study the variability of stars up to 12 mag (Wraight et al. 2011). About 263 EB candidates have been made public after a survey of 650,000 stars with magnitudes brighter than 11.5. The SW is an extrasolar planet detection program hosted by the joint collaboration of eight academic institutes located in the United Kingdom.[3] The SW consists of ground-based robotic observatories and eight wide-angle cameras covering both hemispheres of the sky. The SW-N is located on the island of La Palma among the Isaac Newton Group (ING) of telescopes, and SW-S is at the site of the South African Astronomical Observatory. The operational wavelength band is the entire *V* band covering stars having magnitudes between 8 and 15 and listing several exoplanet candidates, few of which have been speculated by us as potential EB hosts. *Kepler* is a space observatory launched by NASA on 2009 March 7 to discover Earth-like planets orbiting other stars. Along with the usual target list of potential exoplanet host stars, *Kepler* also published a catalog of EB candidates (Koch et al. 2007). The mission is designed specifically to look at around 100,000 stars for transits in the region above the galactic plane looking down at the Orion arm of the Milky Way (Borucki et al. 2009). The aim is to look at the sources that have been flagged as "EB" in the *Kepler* catalog.

One of the four program stars chosen for the study, SAO 106989, is short-listed from the ground-based SW photometry catalog (Street et al. 2007). This source was an exoplanet candidate having a periodicity of 4.4 days and a transit depth of 13.5 mmag. Based on the radius estimation, the secondary was speculated to be a hot Jupiter or an M-dwarf companion (both objects have comparable sizes). HD 24465 and EPIC 211682657 are short-listed from the *K2* photometry database. These candidates are reported to have periodicities of 7.19 and 3.142 days and transit depths of 38 and 46 mmag, respectively (Barros et al. 2016). For HD 24465 and EPIC 211682657, *K2* data are available. The periodicity for HD 205403, which is short-listed from the *STEREO* catalog, is 2.44 days with a transit depth of 57 mmag (Wraight et al. 2012). The stellar parameters for all sources from previous studies are listed in Table 3.

### 2.1. RV Observations

High-resolution spectroscopic observations of the program EBs were taken during 2013–2017 using the optical fiber-fed echelle spectrograph PARAS (high-resolution, $R \sim 67{,}000$, cross-dispersed spectrograph) coupled with the 1.2 m telescope at Gurushikhar, Mount Abu, India. The spectrograph has a spectral coverage of 3800–9000 Å. However, for precise RV measurements, a wavelength range of 3800–6800 Å is utilized. The spectra are recorded in the simultaneous reference mode, wherein one of the two optical fibers is illuminated by the target source and the other is illuminated with thorium–argon (ThAr) as the calibration lamp. The spectrograph is maintained in a temperature-stable (rms of 0.01°C at 25°C) and pressure-stable environment (maximum variation of 0.06 mbar in one night of observation). The nightly calibration sequence includes five bias frames and three flat frames (for which both fibers are illuminated with a tungsten lamp) and several ThAr–ThAr frames (for which both fibers are illuminated with the calibration lamp) throughout the night. The purpose of the ThAr–ThAr frames is to carefully measure absolute instrument drift, as well as differential drifts. Science observations are usually made using simultaneous star–ThAr exposures (two to three exposures per night per target). Details of the spectrograph, observational procedure, and data analysis techniques can be found in Chakraborty et al. (2014).

A total of 17 sets of observations of the source SAO 106989 were acquired between 2013 October and November at a resolving power of 67,000. During 2013, due to telescope tracking issues, it was difficult to keep exposure durations more than 1200 s despite closed-cycle on-axis star guiding. This resulted in signal-to-noise ratios (S/Ns) between 12 and 22 pixel$^{-1}$ at the blaze peak wavelength of the spectrum at 550 nm. This problem of telescope tracking was solved in late 2014, and data taken after that were free from such issues. The source was observed on all nights at an air mass between 1.1 and 1.3. For HD 24465, 14 sets of observations were acquired between 2016 October and December. Based on sky conditions, the exposure duration on most of the nights was 3000 s, whereas for some nights, it was kept at 1800 s, resulting in S/Ns ranging between 13 and 30 pixel$^{-1}$ at the blaze peak wavelength of the spectrum at 550 nm. The air mass throughout the observations for this source was between 1.01 and 1.55. For the source EPIC 211682657, 18 spectra were recorded between the months of 2017 May and November. The S/Ns for these spectra were between 21 and 30 pixel$^{-1}$ at a blaze wavelength around 550 nm with an exposure time of 2400 s. The air mass for the observations on this particular source was between 1.1 and 1.2. In a similar way, HD 205403 was also observed between the months of 2017 May and November. The S/N per pixel at the blaze wavelength around 550 nm for each exposure was between 31 and 40, depending on the exposure times ranging between 1800 and 2400 s. The air mass varied between 1.5 and 1.6 during the course of observations for HD 205403. All nights of observations were spectroscopic in nature, with cloud cover less than ~40% and nightly seeing less than or equal to 2$''$0. A list of epochs and observational details for all stars is shown in Table 1. The first two columns represent the observation time (mid-exposure) in UT and BJD, respectively. The exposure time and observed RV are given in the following columns. The RV errors are limited by photon noise as given by Hatzes & Cochran (1992) as $\sigma_{\rm RV} \sim 1.45 \times 10^9 ({\rm S/N})^{-1} R^{-1} B^{-1/2}$ m s$^{-1}$. Here S/N is the signal-to-noise ratio of the spectra, while $R$ and $B$ are the resolving power and wavelength coverage of the spectrograph in angstroms (Å), respectively. In order to compute the errors on the RV, we randomly varied the signal on each pixel within the Poissonian uncertainty of $\pm\sqrt{N}$, where $N$ is the signal on each pixel, and thereafter computed the cross-correlation function (CCF) for each spectrum. This process is repeated 100 times for each spectrum, and the standard deviation of the distribution of the obtained RV values is given as the 1$\sigma$ uncertainty on the CCF fitting along with the errors from photon noise on each RV point. The computed RV errors are given in the last column of Table 1.

### 2.2. Photometry Observations

In order to determine the radii of both components of the EBs, transit photometry is a suitable technique. All of the stars

[3] https://wasp.cerit-sc.cz

**Table 1**
RV Observations for All Stars: SAO 106989, HD 24465, EPIC 211682657 and HD 205403

| UT Date | T-2,400,000 (BJD-TDB) | Exp. Time (s) | RV (km s$^{-1}$) | $\sigma$-RV (km s$^{-1}$) | UT Date | T-2,400,000 (BJD-TDB) | Exp. Time (s) | RV (km s$^{-1}$) | $\sigma$-RV (km s$^{-1}$) |
|---|---|---|---|---|---|---|---|---|---|
| SAO 106989 | | | | | EPIC 211682657 | | | | |
| 2013 Oct 22 | 56588.193 | 1200 | −16.373 | 0.116 | 2017 May 04 | 57878.130 | 2400 | −21.050 | 0.393 |
| 2013 Oct 22 | 56588.209 | 1200 | −16.566 | 0.086 | 2017 May 04 | 57878.169 | 2400 | −18.993 | 0.535 |
| 2013 Oct 22 | 56588.226 | 1200 | −16.517 | 0.099 | 2017 May 05 | 57879.135 | 2400 | 56.378 | 0.333 |
| 2013 Oct 23 | 56589.180 | 1200 | −6.733 | 0.107 | 2017 May 05 | 57879.164 | 2400 | 58.536 | 0.563 |
| 2013 Oct 23 | 56589.196 | 1200 | −5.638 | 0.151 | 2017 May 06 | 57880.132 | 2400 | 53.411 | 0.485 |
| 2013 Oct 24 | 56590.176 | 1200 | 18.325 | 0.202 | 2017 May 07 | 57881.128 | 2400 | −19.283 | 0.723 |
| 2013 Oct 24 | 56590.193 | 1200 | 19.055 | 0.318 | 2017 May 07 | 57881.158 | 2400 | −20.279 | 0.606 |
| 2013 Oct 24 | 56590.212 | 1200 | 19.362 | 0.215 | 2017 Oct 23 | 58050.483 | 2400 | −8.728 | 0.418 |
| 2013 Oct 25 | 56591.203 | 1200 | 37.663 | 0.102 | 2017 Oct 24 | 58051.465 | 2400 | 9.638 | 0.396 |
| 2013 Oct 25 | 56591.219 | 1200 | 37.857 | 0.113 | 2017 Oct 25 | 58052.474 | 2400 | 78.608 | 0.238 |
| 2013 Oct 25 | 56591.234 | 1200 | 37.813 | 0.160 | 2017 Oct 25 | 58052.497 | 1200 | 77.067 | 0.743 |
| 2013 Oct 26 | 56592.188 | 1200 | −9.680 | 0.098 | 2017 Oct 26 | 58053.441 | 2400 | 6.985 | 0.362 |
| 2013 Oct 26 | 56592.203 | 1200 | −10.613 | 0.133 | 2017 Oct 26 | 58053.481 | 2400 | 1.624 | 0.522 |
| 2013 Oct 26 | 56592.219 | 1200 | −10.016 | 0.214 | 2017 Nov 23 | 58081.369 | 2400 | 41.554 | 0.273 |
| 2013 Oct 27 | 56593.219 | 1200 | −11.047 | 0.191 | 2017 Nov 24 | 58082.372 | 2400 | −20.593 | 0.368 |
| 2013 Oct 27 | 56593.235 | 1200 | −12.113 | 0.192 | 2017 Nov 25 | 58083.867 | 2400 | 57.949 | 0.285 |
| 2013 Nov 19 | 56616.132 | 1200 | 7.089 | 0.052 | 2017 Nov 26 | 58084.369 | 2400 | 55.053 | 0.255 |
| | | | | | 2017 Nov 27 | 58085.363 | 2400 | −18.512 | 0.211 |
| HD 24465 | | | | | HD 205403 | | | | |
| 2016 Oct 20 | 57682.473 | 3000 | −29.703 | 0.047 | 2017 May 03 | 57877.475 | 2400 | −17.531 | 0.118 |
| 2016 Oct 21 | 57683.400 | 3000 | −31.777 | 0.022 | 2017 May 04 | 57878.466 | 2400 | 27.566 | 0.035 |
| 2016 Oct 22 | 57684.425 | 3000 | −26.080 | 0.027 | 2017 May 05 | 57879.471 | 1800 | 25.545 | 0.040 |
| 2016 Oct 24 | 57686.406 | 3000 | 6.609 | 0.033 | 2017 May 06 | 57880.466 | 1800 | −16.253 | 0.101 |
| 2016 Nov 24 | 57717.345 | 1800 | −20.181 | 0.017 | 2017 May 07 | 57881.465 | 2400 | 57.207 | 0.070 |
| 2016 Dec 01 | 57724.412 | 3000 | − 19.660 | 0.015 | 2017 Oct 24 | 58051.169 | 2400 | −24.082 | 0.054 |
| 2016 Dec 02 | 57725.391 | 3000 | −29.201 | 0.011 | 2017 Oct 24 | 58051.211 | 2400 | −25.807 | 0.063 |
| 2016 Dec 03 | 57726.392 | 3000 | −32.479 | 0.014 | 2017 Oct 26 | 58053.143 | 2400 | 17.776 | 0.063 |
| 2016 Dec 04 | 57727.385 | 3000 | −28.576 | 0.013 | 2017 Oct 26 | 58053.176 | 2400 | 12.327 | 0.063 |
| 2016 Dec 05 | 57728.404 | 1800 | −14.190 | 0.012 | 2017 Oct 26 | 58053.207 | 2400 | 9.18 | 0.073 |
| 2016 Dec 06 | 57729.311 | 1800 | 3.471 | 0.015 | 2017 Nov 22 | 58080.113 | 2400 | 8.2811 | 0.052 |
| 2016 Dec 06 | 57729.387 | 1800 | 4.411 | 0.016 | 2017 Nov 23 | 58081.100 | 2400 | −4.205 | 0.053 |
| 2016 Dec 06 | 57729.410 | 1800 | 4.624 | 0.015 | 2017 Nov 23 | 58081.130 | 2400 | −1.091 | 0.063 |
| 2016 Dec 07 | 57730.408 | 1800 | −0.710 | 0.015 | 2017 Nov 24 | 58082.084 | 2400 | 51.576 | 0.052 |
| | | | | | 2017 Nov 24 | 58082.115 | 2400 | 49.116 | 0.052 |
| | | | | | 2017 Nov 25 | 58083.078 | 2400 | −27.789 | 0.053 |
| | | | | | 2017 Nov 25 | 58053.112 | 2400 | −28.016 | 0.053 |
| | | | | | 2017 Nov 26 | 58084.081 | 2400 | 48.109 | 0.063 |
| | | | | | 2017 Nov 26 | 58084.116 | 2400 | 50.53 | 0.073 |
| | | | | | 2017 Nov 27 | 58085.084 | 2400 | 0.055 | 0.063 |
| | | | | | 2017 Nov 27 | 58085.116 | 2400 | −3.132 | 0.073 |

have been observed by ground-based or space-based photometry missions previously. SAO 106989 was first listed as an exoplanet candidate from SW photometry catalogs after surveying millions of stars in the night sky (Street et al. 2007). While the SW photometry has listed many exoplanet candidates in short periods between 2 and 3 days (Street et al. 2007), a periodicity of 4.4 days is relatively long for the catalog's sampling standards. Therefore, due to inadequate time cadence, a smaller number of transit data points is recorded for this source. Moreover, the data for this source look noisy, as seen in Street et al. (2007). However, we found that the source had been observed by the Kilodegree Extremely Little Telescope (KELT) survey (Pepper et al. 2007).[4] KELT consists of two robotic telescopes for conducting a survey for transiting exoplanets around bright stars. The telescope is a wide-field ($26 \times 26$ deg$^2$), small-aperture (42.0 mm) system optimized for imaging bright stars in a broad $R$ band. The telescope is not tracking any field; thus, a single field is imaged for 1–2 hr with an average precision of 7.5 mmag on each observing night. We analyzed the $z$-band image from SDSS-III[5] to check for the possibility of third-light contamination. The SDSS-III images are $6' \times 10'$ and have a plate scale of $0\farcs4$ pixel$^{-1}$ (Gunn et al. 1998). The image is not centered at the source. As seen from Figure 1, we have marked circles of radii 30″, 60″, and 120″ from the center of the source for identifying possible contaminants. There is no contaminant seen within 1′. The nearest source resolved within 2′ is TYC 1658-738-1, which has a magnitude difference of $\Delta V = 2.21$ from our source of interest, SAO 106989. The plate scale of KELT is 23″ pixel$^{-1}$ and a photometric aperture of 3′ (Siverd et al. 2012); a source between 1′ and 2′ could cause slight light contamination, making the photometry data appear noisy.

[4] http://exoplanetarchive.ipac.caltech.edu

[5] http://skyserver.sdss.org/

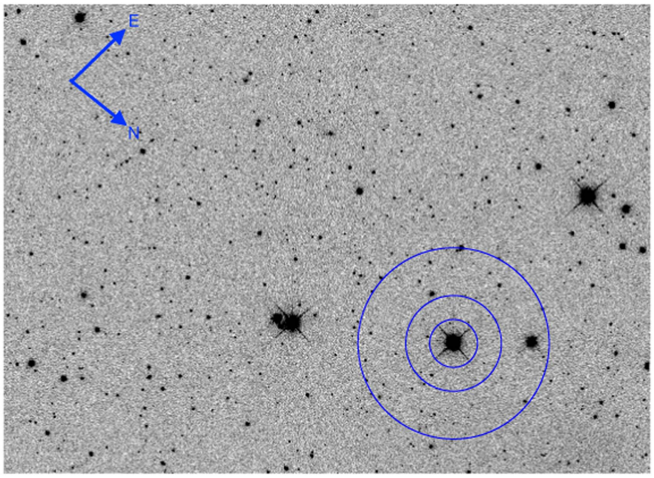


**Figure 1.** SDSS $z$-band image for the source SAO 106989. The radii of the inner, middle, and outer blue circles centered on the source are 30″, 1′, and 2′, respectively. It can be seen that there is no potential source of contamination within 30″. The nearest possible source of contamination ($\Delta V = 2.21$ mag) is between 1′ and 2′.

However, there is no evidence of a photometric dip as predicted during the time of secondary eclipse. This rules out a light-blending scenario, but we would warn readers of light contamination.

HD 24465 and EPIC 211682657 are *K2* candidates. The *Kepler* mission, launched in 2009 (Borucki et al. 2009), led to a surge in the detection of exoplanets and EB candidates. With the *K2* mission, a successor of the *Kepler* mission, the number of detections has grown exponentially, as *K2* observes four fields in 1 yr, and the targets observed are, on average, brighter than the *Kepler* candidates. The photometry data are taken in the *Kepler* filter with a wavelength range between 4200 and 8900 Å ($\lambda_c = 6400$ Å; Brown et al. 2011), timed between 2015 February 08–April 20 for HD 24465 and 2015 April 27–July 10 for EPIC 211682657 with an average photometry precision of 15 ppm. HD 205403 was one of the nine candidates short-listed from the NASA *STEREO* mission as a part of the bright eclipsing candidates (visual magnitude $6 < V < 12$) surveyed by the two satellites onboard the *STEREO* mission looking for stars with effective temperatures between 4000 and 7000 K (Wraight et al. 2012). This program star is an EB candidate, which has a companion radius predicted to be greater than 0.35 $R_\odot$. The star was observed in the wavelength band between 630 and 730 nm with an exposure duration of 40 s. The data were taken every 40 m for the complete duration of 16–17 days when the star was observable on the CCD field of view for each cycle of observation (roughly 1 yr).

## 3. Data Modeling and Results

In this section, we describe the analysis techniques used to reduce the data and the methodology utilized to determine the orbital parameters of the stars studied in this paper.

### *3.1. RV of the Primary Stars of the EB Systems*

The barycentric-corrected RV values and their respective uncertainties are shown in Table 1 for all stars studied in this paper. The phase-folded RV points for all stars are plotted in Figure 2. The figure shows four panels: SAO 106989 at top left, HD 24465 at top right, EPIC 211682657 at bottom left, and HD 205403 at bottom right. The red circles in each panel are the observed RV points, and the solid line is the fitted model for each star, details of which are discussed in Section 3.4. Based on temperatures determined from Section 3.2, SAO 106989 and HD 24465 are found to be F9/G0- and F7/F8-type stars, respectively (Pecaut & Mamajek 2013). Thus, a G2 numerical mask was used as the zero-velocity cross-correlation template to compute RV measurements. The other two stars, EPIC 211682657 and HD 205403, are found to be F4 and F5 type, respectively, based on their temperatures (Pecaut & Mamajek 2013); hence, the F5 numerical mask was used for the cross-correlation.

The data extraction and analysis pipeline (PARAS PIPELINE) is a set of routines written in `IDL` to ease the complex and time-consuming process of data reduction. It is fully automated, requiring a minimal amount of user interaction only if external factors necessitate it. The PARAS PIPELINE is based on the `REDUCE` data analysis package developed by Piskunov & Valenti (2002) for processing cross-dispersed echelle data. It is modified to suit the requirements of the PARAS data. The reduction process requires intake of bias, flat fields, and calibration-lamp frames in unison with the science exposures. Bias frames are for bias corrections, whereas flat frames are for the purpose of order location taken by illuminating the fiber by hot tungsten lamp generally before the science exposures. Wavelength calibration is accomplished by comparing the observed arc-lamp (ThAr for the current case) spectrum with a suitable template spectrum. The wavelength solution was generated for simultaneously illuminated ThAr lamp spectra and can be used as a blueprint solution, as long as external modifications do not affect the fiber and its position. A complete thorium line list for the PARAS spectral range is utilized (similar to the SOPHIE line list at http://www.obs-hp.fr). For the automated process, a binary mask of sharp thorium lines is created and used to assist the calibration process. The CCF is calculated by shifting this thorium mask against each spectral order, and the net drift value is corrected for each spectrum. The extracted wavelength solution is imposed on the observed stellar spectra in the simultaneous reference mode, thereby enabling a wavelength solution for each observed science exposure by incorporating necessary drift corrections. The RVs are finally derived by cross-correlating target spectra, i.e., computing the CCF with a suitable numerical stellar template mask, created especially from high-S/N spectra or synthetic data (Baranne et al. 1996). It consists of values 1 and 0, where nonzero values correspond to the theoretical positions and widths of the absorption lines at zero velocity. The CCF is constructed by shifting the mask as a function of Doppler velocity. The RVs are then corrected for their barycentric velocities. For complete details on the reduction and analysis methods, readers are requested to follow Chakraborty et al. (2014).

### *3.2. Spectral Synthesis*

We utilized the stellar synthesis pipeline, *PARAS SPEC*, to estimate the stellar parameters from the observed spectra (Chaturvedi et al. 2016). Spectra obtained from the instrument are unblazed by fitting a polynomial function and stitched across the echelle orders to produce a single spectrum. Individual spectra are normalized, and many epochs of the same star are coadded after the relevant RV corrections to get a high-S/N continuum-normalized stitched stellar spectrum. This

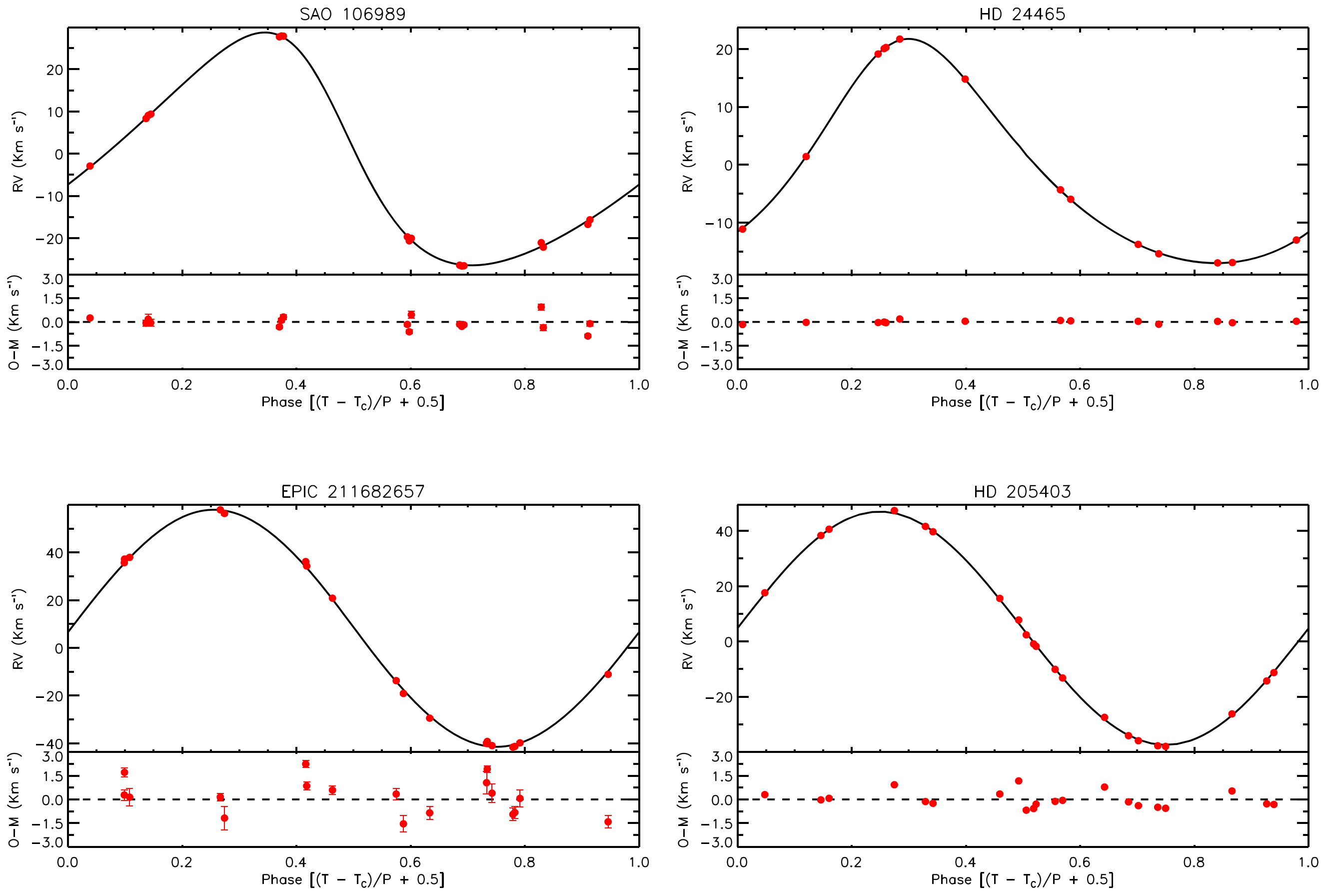


**Figure 2.** Top portion of each panel: RV model curve for SAO 106989 (top left), HD 24465 (top right), EPIC 211682657 (bottom left), and HD 205403 (bottom right) obtained from PHOEBE (see Section 3.4 for details on PHOEBE) plotted against orbital phase. PARAS, Mount Abu (solid red circles), observed data points along with the estimated errors are overplotted on the curve. Bottom portion of each panel: residuals from the best fits plotted below the RV plot. For better visual representation, the *x*-axis in phase is shifted by 0.5 so that the central primary transit crossing point ($T_c$) occurs at phase 0.5 instead of 0.

spectrum serves as input to the stellar pipeline. The observed spectrum needs to be compared against a grid of synthetic spectra. This grid is produced using synthetic spectra generator code SPECTRUM. It utilizes the ATLAS9 models by Kurucz (Kurucz 1993) for stellar atmosphere parameters by working on the principle of local thermodynamic equilibrium and plane-parallel atmospheres. The library consists of synthetic spectra having $T_{\rm eff}$ between 4000 and 7000 K at an interval of 250 K, [Fe/H] in a range of −2.5–0.5 dex with an interval of 0.5 dex, and log *g* between 1.0 and 5.0 dex with an interval of 0.5 dex. The synthetic library generated at this spacing of stellar parameters is a coarse set of libraries. The library can be tuned finer in precision by interpolating the stellar parameters at intermediate values. The wavelength range for the generated synthetic spectra is kept between 5050 and 6560 with an interval of 0.01 Å and a velocity resolution of 1 km s$^{-1}$ between 1 and 40 km s$^{-1}$. *PARAS SPEC* is based on two primary methods, the synthetic spectral-fitting method and equivalent-width method. These two methods and the results obtained after applying them to the target sources are briefly discussed here.

#### *3.2.1. Synthetic Spectral-fitting Method*

The synthetic spectral-fitting method is a four-step automated execution to determine $T_{\rm eff}$, [Fe/H], log *g*, and $v \sin i$. The rms residuals ($\sum(\mathrm{O}(i) - \mathrm{M}(i))^2$) are computed between the observed (O) and modeled (M) spectra at each wavelength bin, $\lambda_i$, in the utilized wavelength region. The model producing the best match with the observed spectra gives the best-fit values of $T_{\rm eff}$, [Fe/H], log *g*, and $v \sin i$. For the first step, all of the parameters are kept free and the maximum wavelength range (5050–6500 Å) is used, as there are many temperature and metallicity lines in this region. The best-fit values of $T_{\rm eff}$, [Fe/H], and $v \sin i$ are stored from this execution and used for the next steps. In the second step, $T_{\rm eff}$ and [Fe/H] are kept frozen and used as an initial guess value, whereas the value of log *g* is kept free. The current step is executed only on the log *g* sensitive Mg I lines in the wavelength region of 5160–5190 Å. The initial two steps are executed on a coarse set of libraries. In order to get better precision on stellar parameters, a finer grid is required to achieve the closest match between the observed and synthetic spectra. Thus, during the course of execution of the synthetic spectral-fitting routine, the synthetic models are interpolated in the desired range of $T_{\rm eff}$, [Fe/H], and log *g* to sharpen the precision of the derived parameters. The interpolation on the models is executed by the IDL subroutine kmod. The interpolated models then have a finer interval in $T_{\rm eff}$ (50 K), [Fe/H] (0.1 dex), and log *g* (0.1 dex). The third step is applied on interpolated models. The parameters obtained from the previous two steps are used as initial guess values, and interpolation is done simultaneously at finer precision. The interpolation is done in the vicinity of the guess values on the three parameters obtained from the first step, i.e., $T_{\rm eff}$ in a range of ±250 K, [Fe/H] in a range of ±0.3, and log *g* in

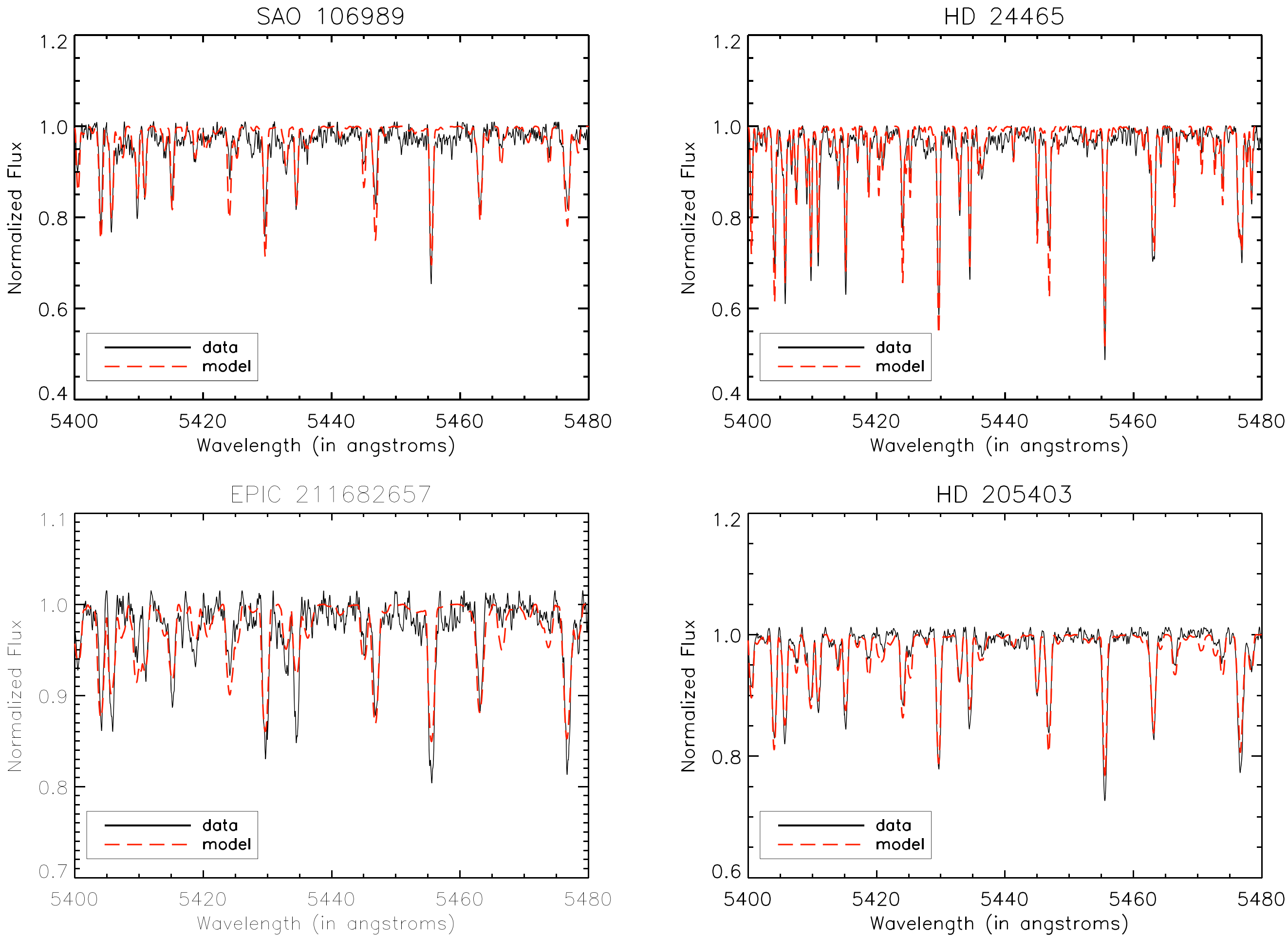


**Figure 3.** The solid line in each panel represents the observed normalized spectra of SAO 106989 (top left), HD 24465 (top right), EPIC 211682657 (bottom left), and HD 205403 (bottom right) plotted across the wavelength region of 5400–5480 Å. Overplotted is the respective modeled spectrum (dashed line) obtained from PARAS SPEC. The stellar parameters for each of the derived models are listed in Table 2. For higher S/Ns, the spectra shown here are smoothed by 1.5 times leading to a resolving power of 44,000. For details, please refer to the text.

a range of ±0.3. The best-determined values of $T_{\rm eff}$ and [Fe/H] derived from this second step are considered initial approximations of the stellar parameters for the last step. The last step is executed for determining the $\log g$ from the wavelength region of 5160–5190 Å on the interpolated models. The $T_{\rm eff}$ and [Fe/H] derived from the third step are used in this last step. This step is similar in execution to the second step, the only difference being that it is applied on an interpolated finer grid. The best-match model determined at this step gives us the value for $\log g$ along with previously determined values of $T_{\rm eff}$ and [Fe/H] from the third step.

For the synthetic spectral-fitting method to work, one needs a high-S/N ($\geqslant$80) observed spectrum. Since all of the program stars studied as a part of this work are of the F spectral type, similar procedures have been adopted for estimating the stellar parameters. We combined all 17 observed epochs (see Table 1) for SAO 106989. The S/N pixel$^{-1}$ in the case of the star SAO 106989 for the combined 17 epochs was ~80–85 in the wavelength region between 6000 and 6500 Å and 55–75 in the wavelength region of 5000–6000 Å. There are prominent metallic lines in the blue region of the spectra for an F-type star. However, this wavelength region of the spectra has less S/N; thereby, in order to effectively use this wavelength region, we smoothed the coadded spectra by a factor of 1.5. This enhanced the S/N to 80–100 in the blue region at a resolving power of ~44,000. Thereby, the wavelength region 5200–5700 Å of the spectra was used for the synthetic spectral-fitting method. The top left panel of Figure 3 shows a sample of the observed spectrum (solid line) overlaid by the best-fit model (dotted line) across the wavelength region 5400–5480 Å. The best-fit stellar parameters for the spectra derived from this method are $T_{\rm eff} = 6000 \pm 100$ K, $[{\rm Fe/H}] = -0.2 \pm 0.1$, and $\log g = 4.2 \pm 0.2$. Similarly, the 14 epochs observed for HD 24465 (see Table 1) were combined and smoothed by a factor of 1.5 for an increased S/N. The combined S/N pixel$^{-1}$ for HD 24465 was found to be ~80–90 in the wavelength region of 6000–6500 Å and between 60 and 80 in the wavelength region of 5000–6000 Å. We used the same wavelength region of 5200–5700 Å for the synthetic spectral fitting. The top right panel of Figure 3 shows a sample of the observed spectrum for HD 24465 (solid line) overlaid by the best-fit model (dotted line). The best-fit derived parameters by *PARAS SPEC* for the model are $T_{\rm eff} = 6250 \pm 100$ K, $[{\rm Fe/H}] = 0.3 \pm 0.15$, and $\log g = 4.0 \pm 0.15$. For EPIC 211682657, we found the S/N pixel$^{-1}$ to be ~70–80 and 65–70 in the wavelength region between 5000–6000 and 6000–6500 Å, respectively, after combining the data for all of the observed 18 epochs (see Table 1) and smoothing to a resolving power of ~44,000. Applying the same routine, we derive the stellar parameters for this star as $T_{\rm eff} = 6650 \pm 125$ K, $[{\rm Fe/H}] = -0.1 \pm 0.15$, and $\log g = 3.8 \pm 0.15$. The bottom left panel of Figure 3 shows the observed spectrum for EPIC 211682657 (solid line) overlaid by the best-fit model (dotted line). Finally, we combined all of the available 21 epochs for HD 205403 (see Table 1) and smoothed the spectra, which resulted in an S/N pixel$^{-1}$ ∼80–90 in the wavelength region between 5000 and 6000 Å and 75–80 in the wavelength region of 6000–6500 Å. The best-fit derived stellar parameters from *PARAS SPEC* are $T_{\rm eff} = 6600$ K, $[{\rm Fe/H}] = -0.1$, and $\log g = 3.5$. The bottom right panel of Figure 3 shows a sample of the observed spectrum (solid line) overlaid by the best-fit model (dotted line). The S/N pixel$^{-1}$ of the combined spectra for all of the stars studied here is, in general, below 100, which causes continuum-matching errors as discussed in Chaturvedi et al. (2016). Thus, the errors on each stellar parameter are found to be relatively larger, of the order of ±75–125 K for $T_{\rm eff}$ and ±0.1–0.15 dex for [Fe/H] and $\log g$.

### 3.2.2. Equivalent-width Method

The equivalent-width (EW) method was used to check and verify results obtained from the synthetic spectral line-fitting method (Blanco-Cuaresma et al. 2014). It works on the principle in which one seeks the neutral and ionized iron lines to satisfy the two equilibria, namely, excitation equilibrium and ionization balance. A set of neutral and singly ionized lines is acquired from the iron line list by Sousa et al. (2014). Identification of unblended lines for determination of EWs is a prerequisite for this method. For this method, similar to the previous method, we utilized the combined higher S/N pixel$^{-1}$ observed spectra. The `SPECTRUM` code facilitates the estimation of the abundance of elements from their spectral lines by using a set of EWs of the fitted lines as an input to the `ABUNDANCE` subroutine. The subroutine also uses various stellar models that are formed as a combination of different $T_{\rm eff}$, [Fe/H], $\log g$, and $v_{\rm micro}$. The main purpose of calculating EW and thereby abundances is the fact that the abundances of a given species follow a set of three golden rules (Neves et al. 2009; Blanco-Cuaresma et al. 2014). This fact can be exploited to choose a best-fit model of synthetic spectra in which all the rules are simultaneously satisfied. These three rules are as follows.

1. Abundances as a function of excitation potential (EP) should have no trends.
2. Abundances as a function of reduced EW (EW/λ) should exhibit no trends.
3. Abundances of neutral iron (Fe I) and ionized iron (Fe II) should be balanced.

For each iteration, abundances are calculated as a function of a set of stellar parameters ($T_{\rm eff}$, $\log g$, and $v_{\rm micro}$). The derived abundances are plotted as a function of EP and reduced EW. Slopes are fitted to these plots by fitting a linear polynomial. A difference of Fe I and Fe II abundances is also calculated for each set of stellar parameters. Both the parameters, $T_{\rm eff}$ and $v_{\rm micro}$, are determined simultaneously by minimized slopes, as mentioned previously. A slight positive or negative slope indicates underestimation or overestimation of $T_{\rm eff}$ and $v_{\rm micro}$ for the star, respectively. Similarly, if the Fe I and Fe II difference is positive or negative, it indicates that $\log g$ is underestimated or overestimated, respectively. The entire process is executed in two steps: the first step is on the coarse grid of models in $T_{\rm eff}$, $\log g$, and $v_{\rm micro}$; the second step is on the interpolated finer grid, similar to the previous method of synthetic spectral fitting. Thus, the model having a set of parameters where the slopes of the iron abundances against EP and reduced EW and the differences between neutral and ionized iron abundances are simultaneously minimized gives us the best-determined $T_{\rm eff}$, $\log g$, and $v_{\rm micro}$.

SAO 106989 has a magnitude of 9.3 and is toward the fainter limit of observations for PARAS. The star has a relatively large rotational velocity (20 km s$^{-1}$) leading to blending of closely situated lines. Thus, there are fewer unblended Fe I and Fe II lines identified for abundance determination by the EW method. In the top left panel of Figure 4, a least-squares fit having a minimum slope for iron abundances versus EP obtained for the best-fit $T_{\rm eff}$ for SAO 106989 is shown in the upper portion of the panel. In the bottom portion, a plot of iron abundance versus reduced EW is shown with a least-squares fit line having a minimum slope for the best-fit $v_{\rm micro}$. HD 24465 has a magnitude of 8.9 and a rotational velocity of 11 km s$^{-1}$. The number of Fe I and Fe II lines identified for abundance determination through EW were sufficient as compared to SAO 106989. In the top right panel of Figure 4, a least-squares fit line having a minimum slope for iron abundances versus EP is obtained for the best-fit $T_{\rm eff}$ for HD 24465, as shown in the upper portion. In the bottom portion, a plot of iron abundance versus reduced EW is shown with a least-squares fit line having a minimum slope for the best-fit $v_{\rm micro}$. EPIC 211682657 has a very large rotational velocity of 40 km s$^{-1}$. Thus, there were no unblended lines available for measurement of EW to determine stellar parameters; hence, the EW method could not be used for this star. The rotational velocity for HD 205403 is 16 km s$^{-1}$. In the bottom panel of Figure 4, a least-squares fit having a minimum slope for iron abundances versus EP obtained for the best-fit $T_{\rm eff}$ for HD 205403 is shown in the upper portion of the panel. In the bottom portion of the panel, a plot of iron abundance versus reduced EW is shown with a least-squares fit line having a minimum slope for the best-fit $v_{\rm micro}$. The spectral properties determined by both methods for all of the program stars are listed in Table 2. We can see from Table 2 that spectral parameters derived from both of these methods agree within the uncertainities given in the table. We have used the average value of the parameters derived by these two methods for further analysis.

## 3.3. Photometry of All of the Primary Stars of the EB Systems

In this section, we describe the retrieval and analysis of the archival data for each of the sources.

We retrieved the reduced data for SAO 106989 from the photometry archives. All of the photometry data available for ∼85 nights between 2007 June 8 and 2008 November 21 were combined to reflect the transit signature, as there were only partial eclipses recorded. Despite the KELT data being noisy for this source, we could fit the light curve at the same period as that for the RV data, as shown in the top left panel of Figure 5.

We retrieve the *K2* self-flat-fielding (K2SFF) correction light-curve data from the MAST Portal[6] for the sources HD 24465 (EPIC 210484192) and EPIC 211682657 from Barros et al. (2016). `The K2SFF` light-curve data are publicly available. The *K2* data are particularly noisy compared to the predecessor *Kepler* data. The technique of aperture photometry and imaging centroid position is applied to account for the spacecraft's motion. This technique incorporates for the

6 https://mast.stsci.edu/portal/Mashup/Clients/Mast/Portal.html

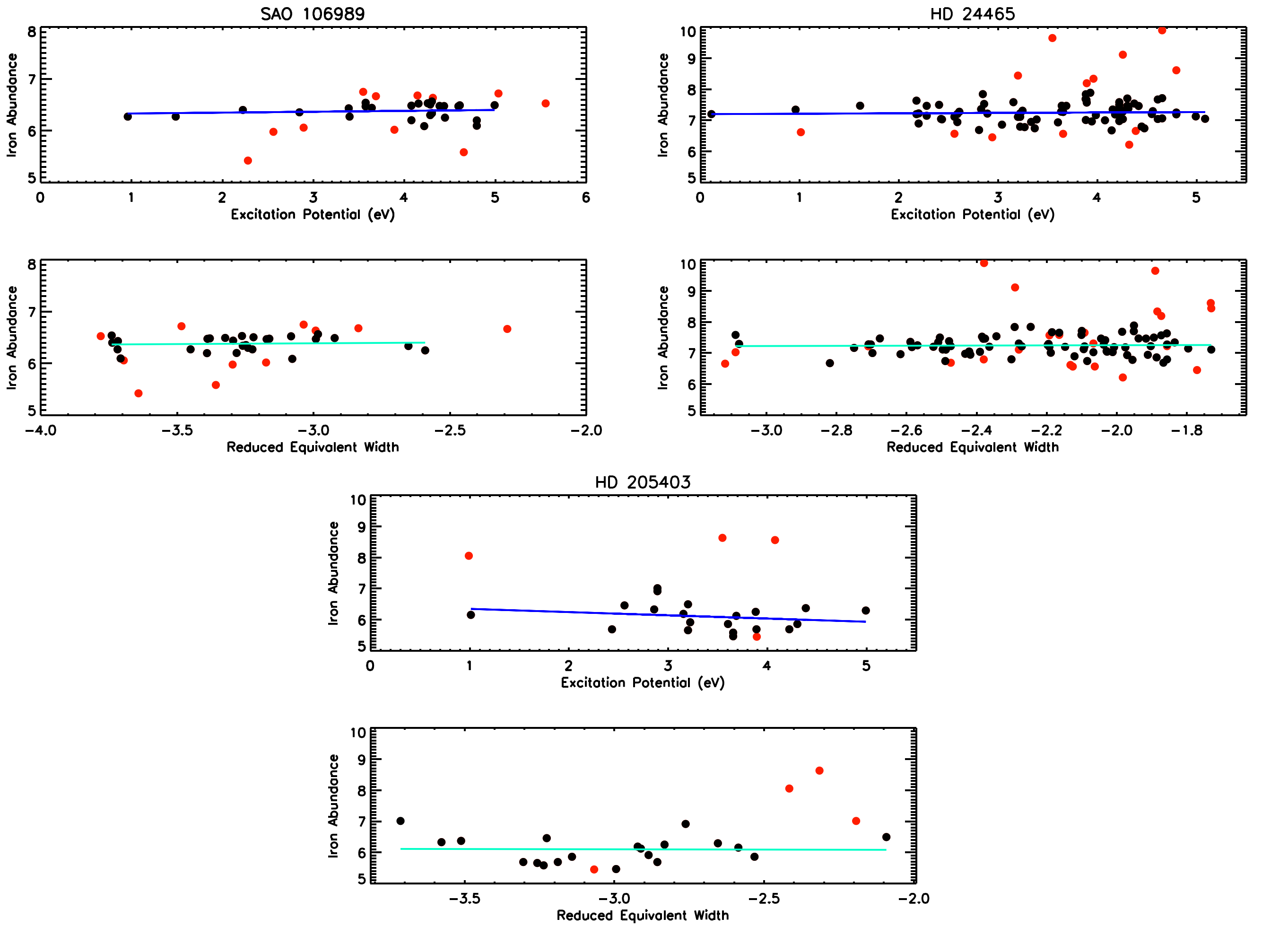


**Figure 4.** The top portion of each panel is the iron abundance for SAO 106989 (top left), HD 24465 (top right), and HD 205403 (bottom) plotted against EP for each Fe I or Fe II line from the line list. The blue line is the least-squares fit to each data point seen in the scatter plot indicating the minimum slope for the best-determined $T_{\rm eff}$. In the bottom portion of each panel, iron abundance is plotted against reduced EW, and the cyan line indicates the minimum slope for the least-squares fit obtained on the data for the best-determined $v_{\rm micro}$ for each of the stars. The red points are the discarded points having a standard deviation beyond $1\sigma$ (not considered for the fit). The stellar parameters for each of the derived models are listed in Table 2.

nonuniform pixel response function of the *K2* detectors by correlating the measured flux with the spacecraft's pointing angle and correcting for such dependence (Vanderburg & Johnson 2014). Data points with poor photometric performance are removed, and variabilities of the order of 6 hr caused by spacecraft jitter are also removed. The B spline function is fitted iteratively to the data points in order to eliminate low-frequency variability. The acquired data for both stars are long-cadence data with an average time cadence of 30 minutes. We could detect 23 complete eclipses for EPIC 211682657 and 10 eclipses for HD 24465 for ~75 nights of observation for each of the fields. The photometry data and the period determined by the RV data agree well with each other. The transit data fitted at the orbital period of 7.197 and 3.142 days for HD 24465 and EPIC 211682657 are shown, respectively, in the top right and bottom left panels of Figure 5.

For the EB HD 205403, *STEREO* data from the HI-1A instrument were extracted from the UK Solar System Data Centre website.[7] We extracted the available bias-subtracted and flat-fielded data between 2008 December and 2010 November, which constituted eight complete transit events for ~35 nights of observation for the two cycles. The spacecraft coordinates were converted to sky coordinates to identify the star. We used the standard IRAF[8] DAOPHOT package for processing the photometry data and continuum normalized for light-curve fitting. Aperture photometry was applied for different aperture sizes of 2.5, 3.0, and 3.5 pixels around the star. A larger aperture included too much background contribution, and a smaller aperture had the starlight spill over the aperture in some of the frames. Thus, an aperture of 3 pixels was found appropriate. Sky background was calculated between pixel radii 7.0 and 10, as there was no contamination from neighboring sources. Photon–electron conversion gain for the camera was kept at 15 units (Sangaralingam & Stevens 2011). The rms scatter on the light curve for the source star outside the transit time duration is 7 mmag. The photometry data fitted and phase-folded at a period of 2.44 days and our matched RV-derived period are shown in the bottom right panel of Figure 5. We also searched for the secondary eclipse but did not find any significant evidence. The secondary eclipse depths for all of the sources were either undetectable or small. The data for

[7] www.ukssdc.rl.ac.uk

[8] IRAF is distributed by the National Optical Astronomy Observatory, which is operated by the Association of Universities for Research in Astronomy, Inc., under cooperative agreement with the National Science Foundation.

Table 2
Spectral Properties of All Primary Stars Derived by *PARAS SPEC*

| Parameters | Synthetic Spectral Fitting | EW Method |
|---|---|---|
| SAO 106989 | | |
| $T_{\rm eff}$ (K) | 6000 ± 100 | 5925 ± 100 |
| [Fe/H] | −0.2 ± 0.1 | −0.2 (fixed) |
| log $g$ | 4.2 ± 0.2 | 4.25 ± 0.1 |
| $v_{\rm micro}$ (km s$^{-1}$) | … | 0.5 ± 0.1 |
| $v \sin i$ (km s$^{-1}$) | 20 ± 2 | … |
| HD 24465 | | |
| $T_{\rm eff}$ | 6250 ± 100 | 6150 ± 75 |
| [Fe/H] | 0.3 ± 0.15 | 0.3 (fixed) |
| log $g$ | 4.0 ± 0.15 | 4.06 ± 0.1 |
| $v_{\rm micro}$ (km s$^{-1}$) | … | 0.5 ± 0.1 |
| $v \sin i$ (km s$^{-1}$) | 11 ± 1 | … |
| EPIC 211682657 | | |
| $T_{\rm eff}$ | 6650 ± 125 | … |
| [Fe/H] | −0.1 ± 0.15 | … |
| log $g$ | 3.8 ± 0.15 | … |
| $v \sin i$ (km s$^{-1}$) | 40 ± 1 | … |
| HD 205403 | | |
| $T_{\rm eff}$ | 6600 ± 100 | 6450 ± 75 |
| [Fe/H] | −0.1 ± 0.15 | −0.1 (fixed) |
| log $g$ | 3.5 ± 0.15 | 3.7 ± 0.1 |
| $v_{\rm micro}$ (km s$^{-1}$) | … | 1.4 ± 0.1 |
| $v \sin i$ (km s$^{-1}$) | 25 ± 1 | … |

**Note.** Note that the EW method could not be applied for EPIC 211682657. For details, please refer to the text.

SAO 106989 are not modeled by the PHysics Of Eclipsing BinariEs (PHOEBE) for secondary eclipse, as the data were significantly noisy. The secondary eclipse depths for HD 24465 and EPIC 211682657 as modeled from *Kepler* data are 0.000018 and 0.009 (in normalized flux units), respectively. For the source HD 205403, the secondary eclipse depth is 0.0088, but the standard deviation for out-of-transit points is 0.0108 and thus undetectable.

### *3.4. Orbital Parameters for SAO 106989, HD 24465, EPIC 211682657, and HD 205403*

We utilized PHOEBE (Prša & Zwitter 2005) for the modeling of the light curves and RV data for the four EBs SAO 106989, HD 24465, EPIC 211682657, and HD 205403. The routine is based on the WDs differential corrections method of Wilson & Devinney (1971) using Nelder and Mead's downhill simplex for minimization based on function evaluations. The routine reads the photometry and RV data, a set of initial parameters depending on the physical and geometrical properties of the system, and the minimization algorithm needed for the process. PHOEBE has a back-end scripter that can facilitate the implementation of heuristic scans of the solutions to probe the parameter degeneracies and avoid local minima (Gomez Maqueo Chew 2010). Heuristic scanning offers improvisation to minimization algorithms by selecting starting points in parameter hyperspace and minimizing from each point. The obtained parameters are weighted appropriately by sorting solutions based on cost function. Simulated annealing is another method used to avoid local minima (Prša & Zwitter 2005).

We have extensively referred to the Gomez Maqueo Chew (2010) thesis for developing a methodology to extract optimum system parameters for the EBs in consideration. A model-detached, contact or semicontact binary for the system has to be chosen in the interface menu based on an understanding of the general physics and geometry of the system. Stellar surfaces are considered as equipotential surfaces best described by a Roche model. The surface potentials determine the shape and size of the components (Kallrath & Milone 2009). The algorithm initially uses only RV data to fix RV-dependent orbital parameters. The mid-transit time $T_0$, orbital period $P$, and angle of inclination $i$ are kept fixed for this iteration. The RV data are fitted independently to constrain the mass ratio $q$, semi-RV amplitude $K$, semimajor axis as a function of angle of inclination $a \sin i$, eccentricity $e$, angle of periastron $\omega$, phase shift $\phi$, and line-of-sight velocity $v_\gamma$ by using differences of convex functions (DC) minimization. A single iteration gives some solution parameters that are returned for the user to inspect. Each time these parameters are resubmitted to improve the quality of the RV fit, thereby minimizing the cost function ($\chi^2$) of the solution. The cost function converges and free parameters do not change within the error limits. This is the time one stops iterating the system any further. The values obtained from the RV iteration are noted and used for further analysis. The second part involves the fitting of light-curve data, keeping the RV-obtained parameters fixed. PHOEBE supports linear, logarithmic, and square-root limb-darkening (LD) laws. We utilize the logarithmic ones for the case of the optical wavelength regime, as it suits the best. The LD coefficients are modified dynamically by using van Hamme (1993) tables and linearly interpolated to obtain appropriate values. The primary temperature of the system $T_{\rm eff_1}$ is kept fixed and derived from spectral analysis. The parameters $i$, primary surface potential $\Omega_1$, secondary surface potential $\Omega_2$, and secondary temperature $T_{\rm eff_2}$ are kept free for fitting.

We fixed the albedo and gravity-brightening coefficients at 0.5 and 0.32, respectively, for both components, as both the primary and secondary stars here have convective envelopes ($T_{\rm eff} < 7200$ K; Zasche 2016). We also assumed both components of the system to be synchronous. Similar to the RV iteration, light-curve iteration is executed until the cost function is minimized within the error bars of the free parameters. After each iteration, the value of $a \sin i$ is updated. The parameters $e$, $\omega$, and $\phi$ depend on both RV and light-curve data. Finally, RV and photometry data are fitted simultaneously to obtain a single consistent solution. The error bars on each derived quantity are obtained by the method of error propagation discussed in Gomez Maqueo Chew (2010). The values, along with their respective error bars obtained for the orbital parameters, are summarized in Table 3. The error bars are estimated using linear propagation of errors. We have flagged the values in Table 3 that are derived using error propagation. These parameters for which error propagation is used to estimate uncertainties are derived parameters and not fitted parameters. The formal errors derived by us on mass and radius range from 1% to 3% and 0.5% to 3%, respectively. These numbers, when compared to the intrinsic scatter on mass and radius seen from the Torres et al. (2010) relation, are 6.4% and 3.2%, respectively. Thus, we see that formal uncertainties are smaller than the scatter in the Torres relation. This implies that the intrinsic scatter in the Torres relation dominates the uncertainty on mass and radius derived by measurements. It will be imperative in the near future to work toward reducing this scatter in the empirical Torres relation for more reliable estimates of the masses and radii of EB components. It is important to note that the literature-based radius value of the

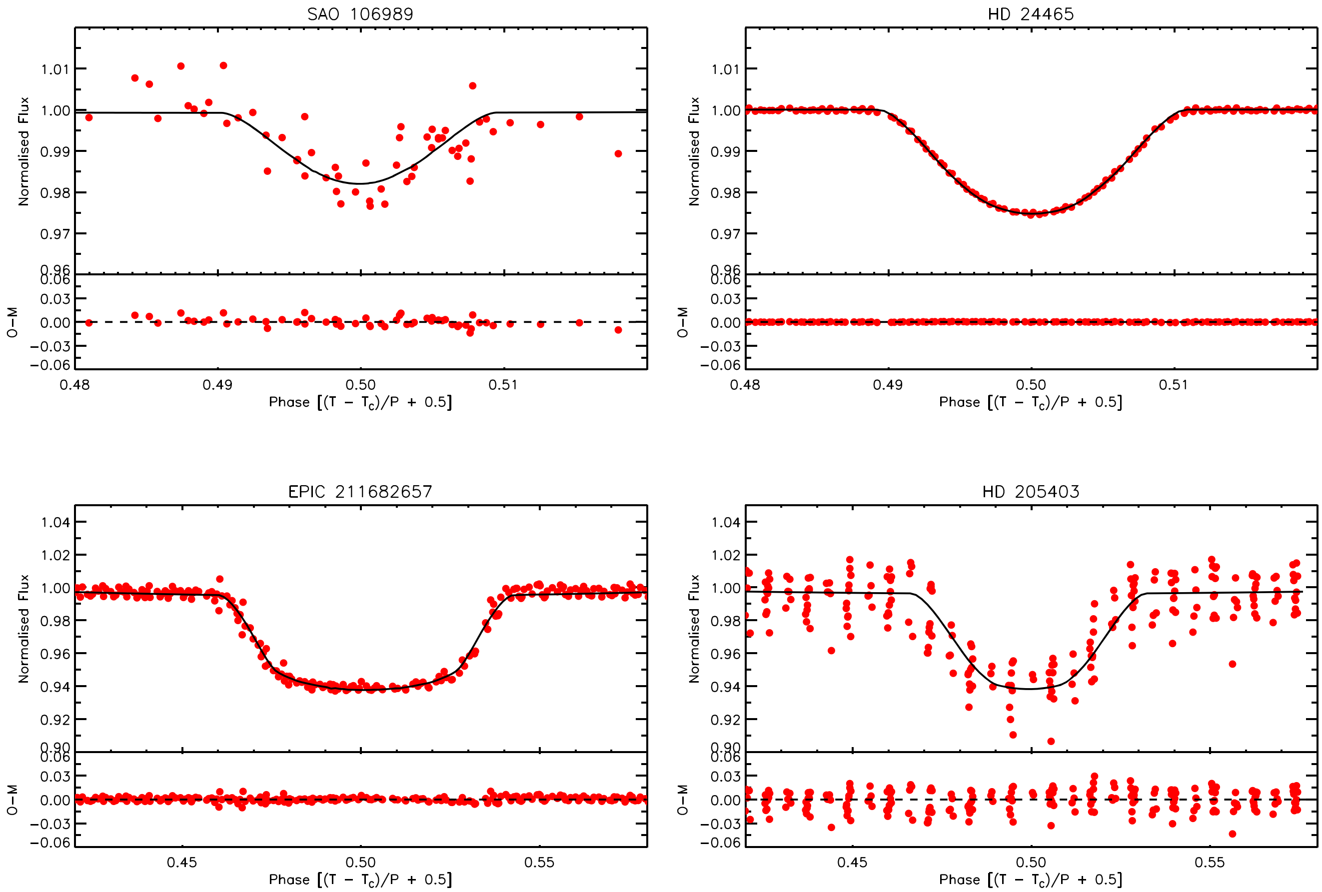


**Figure 5.** Top portion of each panel: transit curve (filled circles) for SAO 106989 obtained from KELT data (top left), HD 24465 obtained from *K2* data (top right), EPIC 211682657 obtained from *K2* data (bottom left), and HD 205403 obtained from *STEREO* data (bottom right) plotted based on the parameters derived from PHOEBE with a solid line. (Refer to Section 3.4 for details on PHOEBE.) Bottom portion of each panel: observed-fit residuals. For better visual representation, the *x*-axis in phase is shifted by 0.5 so that the central primary transit crossing point ($T_c$) occurs at phase 0.5 instead of 0.

primary is derived from the photometric temperature of the primary for SAO 106989 and HD 205403. These radius values are further used to derive the secondary radius values based on the transit depth. Since the available data for both SAO 106989 and HD 205403 are taken from ground-based photometry, the radii derived from photometric methods have significant differences from the values derived by us, which are based on a detailed analysis using photometry data in unison with spectroscopy methods and the Torres relation.

### 3.4.1. SAO 106989

The periodicity for SAO 106989 of 4.39790 ± 0.00001 days obtained from the analysis is close to the value obtained from SW photometry. The RV semi-amplitude for the EB system is 26.189 ± 0.251 km s$^{-1}$ with an eccentricity of 0.248 ± 0.005 at an orbital separation of 0.0583 ± 0.0005 au. The top left panel of Figure 2 illustrates the RV-versus-orbital phase for SAO 106989. Solid red circles (top portion) show the RV measurements of the star taken with PARAS. The figure also shows the residuals (observed-model) in the bottom portion of the panel. The *PARAS SPEC* routine applied on SAO 106989 gives $T_{\rm eff} = 5963 \pm 100$ K, [Fe/H] $= -0.2 \pm 0.1$, and $\log g = 4.23 \pm 0.1$. (The *PARAS SPEC* results for all sources studied here are the mean of the results obtained from the synthetic spectral-fitting and EW methods.) The mass and radius for the primary of the EB system SAO 106989 based on the spectroscopic analysis and Torres relation (Torres et al. 2010) are 1.111 ± 0.27 $M_\odot$ and 1.369 ± 0.111 $R_\odot$, respectively. The mass of the secondary derived from RV data is 0.256 ± 0.005 $M_\odot$, determined at an accuracy of ∼3% (formal errors). The radius value predicted for SAO 106989B from SW photometry is $R_B = 0.126\,R_\odot$. This is much lower than the theoretically expected radius value derived for a star having a mass of $M_B = 0.256\,M_\odot$. However, we retrieved KELT data and performed detailed transit modeling. Despite the data being slightly noisy, we could simultaneously fit the transit obtained from KELT light curves. The top left panel of Figure 5 (upper portion) shows the simultaneous fit for the transit light curve obtained by using the KELT light curve (filled circles) overplotted with the model derived from PHOEBE (solid curve), with residuals plotted in the lower portion of the panel. The simultaneous fit gives us a transit depth of 0.063 ± 0.002 mag and angle of inclination of 81°.624 ± 0°.547. The radius determined through observations is 0.326 ± 0.012 $R_\odot$.

### 3.4.2. HD 24465

HD 24465 is a short-period EB candidate by *K2* photometry having a transit depth of 38 mmag (Barros et al. 2016). We confirmed the orbital period of this EB at 7.19635 ± 0.00002 days with PARAS RV data. The RV semi-amplitude for the EB system is 18.629 ± 0.053 km s$^{-1}$ with an eccentricity of 0.208 ± 0.002 at an orbital separation of 0.0849 ± 0.0002 au.

**Table 3**
Median Values Obtained from Simultaneous RV and Transit Fitting for SAO 106989, HD 24465, EPIC 211682657, and HD 205403

| Parameter | Units | SAO 106989 | HD 24465 | EPIC 211682657 | HD 205403 | Reference |
|---|---|---|---|---|---|---|
| Primary: | | | | | | |
| $V$ mag | | 9.3 | 8.98 | 8.69 | 8.03 | SIMBAD |
| Sp. Type | | F7 | F8 | F2 | F2/F3 | SIMBAD |
| R.A. | WCS | $21^h16^m45^s.22$ | $03^h54^m03^s.3689$ | $08^h54^m33^s.0267$ | $21^h35^m03^s.7303$ | SIMBAD |
| Decl. | WCS | $+19^d21^m36^s.79$ | $+15^d08^m30^s.12$ | $+15^d40^m55^s.030$ | $-03^d44^m05^s.691$ | SIMBAD |
| $M_A$ | $M_\odot$ | 1.11 ± 0.22[a] | 1.337 ± 0.008[a] | 1.721 ± 0.047[a] | 1.445 ± 0.019[a] | This work |
| $R_A$ | $R_\odot$ | 1.24 | ⋯ | ⋯ | 1.46 | S07, W12 |
| $R_A$ | $R_\odot$ | 1.369 ± 0.093[a] | 1.444 ± 0.004[a] | 2.574 ± 0.024[a] | 1.857 ± 0.038[a] | This work |
| $\Omega_1$ | | 9.47 ± 0.31 | 5.988 ± 0.010 | 5.0155 ± 0.113 | 5.349 ± 0.101 | This work |
| log $g_A$ | cgs | 4.211 ± 0.127[a] | 4.245 ± 0.0036[a] | 3.852 ± 0.015[a] | 4.060 ± 0.032[a] | This work |
| $T_{\rm eff,\ A}$ | K | 6000 ± 100 | 6250 ± 100 | 6650 ± 150 | 6600 ± 100 | This work |
| [Fe/H] | | −0.2 ± 0.1 | 0.30 ± 0.15 | −0.1 ± 0.15 | −0.100 ± 0.15 | This work |
| Secondary: | | | | | | |
| $e$ | | 0.248 ± 0.005 | 0.208 ± 0.002 | 0.0097 ± 0.0008 | 0.002 ± 0.002 | This work |
| $\Omega_2$ | | 10.552 ± 1.46 | 14.663 ± 0.056 | 8.6954 ± 0.0167 | 7.299 ± 0.686 | This work |
| $\omega_*$ | rad | 1.035 ± 0.065 | 5.988 ± 0.010 | 0.89 ± 0.06 | 5.603 ± 0.165 | This work |
| $P$ | days | 4.400381 | 7.1977 | 3.141 | 2.4449±0.0005 | S07, B16, W12 |
| $P$ | days | 4.39790 ± 0.00001 | 7.19635 ± 0.00002 | 3.142023 ± 0.000003 | 2.444949 ± 0.000001 | This work |
| $a \sin i$ | au | 0.0583 ± 0.0005 | 0.0849 ± 0.0002 | 0.0556 ± 0.0005 | 0.0438 ± 0.0001 | This work |
| $M_B$ | $M_\odot$ | 0.256 ± 0.005[a] | 0.233 ± 0.002[a] | 0.599 ± 0.017[a] | 0.406 ± 0.005[a] | This work |
| $R_B$ | $R_\odot$ | 0.123 | ⋯ | ⋯ | $\gtrsim$0.35 | S07, W12 |
| $R_B$ | $R_\odot$ | 0.326 ± 0.012[a] | 0.244 ± 0.001[a] | 0.566 ± 0.005[a] | 0.444 ± 0.014[a] | This work |
| $T_{\rm eff,\ B}$ | K | 2380.28 ± 259.39 | 2335.6 ± 8.56 | 4329.0 ± 49.42 | 4651 ± 123.33 | This work |
| log $g_B$ | cgs | 4.818 ± 0.128 | 5.029 ± 0.007 | 4.711 ± 0.015 | 4.752 ± 0.033 | This work |
| RV: | | | | | | |
| $K$ | km s$^{-1}$ | 26.189 ± 0.251[a] | 18.629 ± 0.053[a] | 49.691 ± 0.636[a] | 42.7785 ± 0.2627[a] | This work |
| $M_B/M_A$ | | 0.230 ± 0.002 | 0.174 ± 0.008 | 0.3481 ± 0.004 | 0.2861 ± 0.0053 | This work |
| $M \sin^3 i$ | $M_\odot$ | 1.324 ± 0.027[a] | 1.560 ± 001[a] | 2.312 ± 0.063[a] | 1.7986 ± 0.0234[a] | This work |
| $\gamma$ | km s$^{-1}$ | 2.801 ± 0.154 | −15.800 ± 0.029 | 28.629 ± 0.336 | 14.745 ± 0.132 | This work |
| Age[b] | Gyr | ∼2 | ∼2.3 | ∼1.4 | ∼1.2 | This work |
| Transit: | | | | | | |
| $T_C$ | BJD | 2456595.968 ± 0.028 | 2457097.860675 ± 0.004145 | 2457880.386430 ± 0.009466 | 2457878.9245 ± 0.0325 | This work |
| $i$ | deg | 81.624 ± 0.547 | 86.267 ± 0.013 | 87.113 ± 0.037 | 82.103 ± 0.146 | This work |
| $\delta$ | mag | 0.0135 | 0.038 ± 0.002 | 0.050 ± 0.0006 | 0.057 ± 0.014 | S07, B16, W12 |
| $\delta$ | mag | 0.063 ± 0.002 | 0.0315 ± 0.0005 | 0.053 ± 0.001 | 0.063 ± 0.003 | This work |
| $T_{14}$ | min | 145 | 263 ± 14 | 375 ± 5 | ⋯ | S07, B16 |

**Notes.** It also includes data taken from the literature for the respective sources; SAO 106989 by SW photometry as discussed in Street et al. (2007) (S07); HD 24465 and EPIC 211682657 by *K2* data as discussed in Barros et al. (2016) (B16); and HD 205403 by *STEREO* data from Wraight et al. (2012) (W12). (The transit duration for HD 205403 was not mentioned in literature by Wraight et al. 2012. Similarly, the information on the radii of the primary and secondary components of EBs HD 24465 and EPIC 211682657 was not given in Barros et al. 2016. These places are thus indicated by blanks in the table).
[a] Uncertainities estimated using the error propagation.
[b] Average stellar age determined isochronically and gyrochronically. See Section 4.

The top right panel of Figure 2 illustrates the RV-versus-orbital phase for HD 24465. The *PARAS SPEC* routine applied to HD 24465 gives $T_{\rm eff} = 6200^{+76}_{-81}$, [Fe/H] $= 0.30 \pm 0.14$, and $\log\ g = 4.03 \pm 0.15$. Based on the stellar parameters derived and application of the Torres relation (Torres et al. 2010), the mass and radius for HD 24465A are derived as $1.337 \pm 0.008\,M_\odot$ and $1.444 \pm 0.003\,R_\odot$, respectively. The top right panel of Figure 5 (upper portion) shows the simultaneous fit for the transit light curve obtained by using *K2* data (filled circles) overplotted with the model derived from PHOEBE (solid curve), with the residuals plotted in the lower portion of the panel. The simultaneous fit gives us a transit depth of $0.03145 \pm 0.0005$ mag and angle of inclination of $86^\circ.267 \pm 0^\circ.013$. The mass and radius of the secondary derived here are $0.233 \pm 0.002\,M_\odot$ and $0.244 \pm 0.001\,R_\odot$, determined at an accuracy of ∼1% (formal errors).

### 3.4.3. EPIC 211682657

EPIC 211682657 is an EB with a periodicity of $3.142023 \pm 0.000003$ days reported by *K2* photometry, which was confirmed by us with the RV data. The RV semi-amplitude for the EB system is $49.691 \pm 0.636$ km s$^{-1}$ with a small eccentricity of $0.0097 \pm 0.0008$. The EB has an orbital separation of $0.0556 \pm 0.0005$ au. The bottom left panel of Figure 2 illustrates the RV-versus-orbital phase for EPIC 211682657. The *PARAS SPEC* routine applied to EPIC 211682657 gives $T_{\rm eff} = 6650 \pm 125$, [Fe/H] $= -0.1 \pm 0.15$, and $\log g = 3.8 \pm 0.15$. The mass and radius derived for the primary star of the EB EPIC 211682657 are $1.721 \pm 0.048\,M_\odot$ and $2.574 \pm 0.024\,R_\odot$, respectively (Torres et al. 2010). The bottom left panel of Figure 5 (upper portion) shows the simultaneous fit for the transit light curve obtained by using *K2* data (filled circles) overplotted with the model derived from PHOEBE (solid curve). The residuals are plotted in the lower portion of the panel. We determine a transit depth of 0.053 ± 0.0008 mag and angle of inclination of 87°.113 ± 0°.0368 from the simultaneous fit. The mass and radius of EPIC 211682657B based on the combined fit are 0.599 ± 0.017 $M_\odot$ and 0.566 ± 0.005 $R_\odot$, respectively, derived at an accuracy of ~1% (formal errors).

### 3.4.4. HD 205403

HD 205403 is another short-period EB with a periodicity of 2.444949 ± 0.000001 days as mentioned by Wraight et al. (2012) from *STEREO* photometry. We retrieved the *STEREO* archival data and confirmed the periodicity with the transit data, as well as the RV data of PARAS. The RV semi-amplitude for the primary of the HD 205403 EB system is 42.7785 ± 0.2627 km s$^{-1}$, with a near-circular orbit having an eccentricity of 0.002 ± 0.002. The two stars of the EB are separated by 0.0438 ± 0.0001 au. The bottom right panel of Figure 2 illustrates the RV plotted against orbital phase for HD 205403. The *PARAS SPEC* routine applied to HD 205403 gives $T_{\rm eff}$ = 6525 ± 100, [Fe/H] = 0.1 ± 0.14, and log $g$ = 3.6 ± 0.15. The Torres relation (Torres et al. 2010) applied to HD 205403A gives us the mass and radius as 1.445 ± 0.089 $M_\odot$ and 1.857 ± 0.038 $R_\odot$, respectively. The bottom right panel of Figure 5 (upper portion) shows the simultaneous fit for the transit light curve obtained by using *K2* data (filled circles) overplotted with the model derived from PHOEBE (solid curve), with residuals plotted in the lower portion of the panel. The RV and photometry data are fitted simultaneously, giving us a transit depth of 0.063 ± 0.0027 mag and angle of inclination of 82°.103 ± 0°.146. We determine the mass and radius of the secondary as 0.406 ± 0.005 $M_\odot$ and 0.444 ± 0.014 $R_\odot$, respectively. The accuracy for determination of mass and radii is ~6% (formal errors).

## 4. Discussion

### 4.1. Tidal Evolution in EBs

The primary stars for all the EBs, SAO 106989, HD 24465, EPIC 211682657, and HD 205403, are F-type primaries. The F-type stars act as a bridge between solar-type stars having large convective envelopes and early-type stars having radiative envelopes. Stars having larger convective zones suffer faster tidal dissipation than those having outer radiative envelopes (Zahn 1977). Turbulent friction acting on the equilibrium tide acts on the convective zones, whereas radiative damping of the dynamical tide on the radiative zones is the chief progenitor for tidal dissipation (Zahn 2008). The nature of tidal interaction depends more on the separation of the two components than their sizes (Ogilvie 2014). The tidal forces work in the direction to synchronize spin and angular velocities through an exchange of angular momentum and the dissipation of energy, alignment of spin axis perpendicular to orbital plane, and circularization of the binary orbit (Mathis & Le Poncin-Lafitte 2009). Tides caused by close-in companions pose a threat to the existence of the binary system in a few cases. If the spin of the primary star is slower than the binary orbital period, the tidal torque raised by the companion will spin up the primary. In order to conserve angular momentum, the semimajor axis of the companion will decrease, resulting in an inward spiraling of the companion toward the primary. This happens to G- and K-type primaries, whereas for F-type primaries, the spin period is sufficiently high to evade this engulfment (Bouchy et al. 2011a, 2011b; Poppenhaeger 2017). This is the main reason we see F+M systems commonly in nature.

The rotational velocity ($v \sin i$) of SAO 106989 is ~20 km s$^{-1}$, as computed from the RV CCF. We assumed here that the primary star's rotation axis is aligned with the orbital inclination. Thus, this is the minimum rotational velocity inferred for the star, and the rotational period derived from here will be maximum. In Figure 1 of Meibom et al. (2015), the authors compared the rotational periods, temperatures, and ages of stars. We use the rotational period of SAO 106989 to estimate the age of the EB to be between 0.7 and 1 Gyr. The second source, HD 24465, has a higher temperature than SAO 106989 but a smaller rotational velocity of ~11 km s$^{-1}$, as computed from the CCF width. We thereby estimate an age of ~2 Gyr on account of the rotational period of the star. This age is more than that of SAO 106989; thereby, we conclude that HD 24465 has slowed down based on its age. The next source, EPIC 211682657, is an early F-type star having a higher temperature than the other two stars discussed. It has a large rotational velocity of ~40 km s$^{-1}$, as computed from CCF width. We similarly derive an age of ~1.0 Gyr for this EB based on the rotational period of the primary star. Finally, HD 205403 is also a mid-F-type star like EPIC 211682657. It has a temperature close to 6500 K. It has a rotational velocity of ~25 km s$^{-1}$, and thereby we derive an age of ~1.0 Gyr for this EB. We also utilized the publicly available ISOCHRONES package (Morton 2015) to determine the age of these EB systems. We used Dartmouth stellar evolution tracks (Dotter et al. 2008) for the models and provided the stellar parameters (for the primary star), $T_{\rm eff}$, [Fe/H], and log $g$ derived from Section 3.2. The photometric magnitudes in different bands ($B$, $V$, $J$, $H$, and $K$) were taken from SIMBAD. The ages derived from these isochrones are 3.047 ± 0.85 and 2.517 ± 0.45 Gyr for SAO 106989 and HD 24465, respectively. Similarly, the ages of EPIC 211682657 and HD 205403 are 1.705 ± 0.393 and 1.44 ± 0.207 Gyr, respectively. The ages inferred from the rotational periods of the EBs and those derived by the Dartmouth stellar evolution tracks more or less agree for all the EBs, except for SAO 106989. The age of SAO 106989 derived from its rotational period is almost three times shorter than that derived from the ISOCHRONES package. However, for stars in close binary systems, the tides generated by the M-dwarf companion may spin up the primary star, SAO 106989A. Thus, the rotational velocity of SAO 106989A would be larger, and thereby its rotational period is smaller than if the star had been isolated. The ages of the systems that we used for further analysis are the average of those derived by the above two methods, as indicated in Table 3.

Synchronization of orbital and rotational velocities is an indication of stable evolution of the orbit of the system (Hut 1981). Several of binaries are studied for their synchronization and circularization timescales (Claret et al. 1995; Meibom et al. 2006). For stars with convective envelopes (mass $\leqslant 1.6\, M_\odot$) and solar ages, Zahn (1977) assumed that the primary star rotates uniformly with an angular velocity $\omega$ and its spin axis is perpendicular to the orbital plane in a similar reference frame corotating with the star. The authors derived the synchronization timescales in years as given by the equation $t_{\rm sync} \sim q^{-2}(a/R)^6 \sim 10^4((1+q)/2q)^2 P^4$. Here $q$ is the mass ratio of the two stars, $a$ is the orbital separation, $R$ is the radius of the primary star, and $P$ is the orbital period of the system. We used the

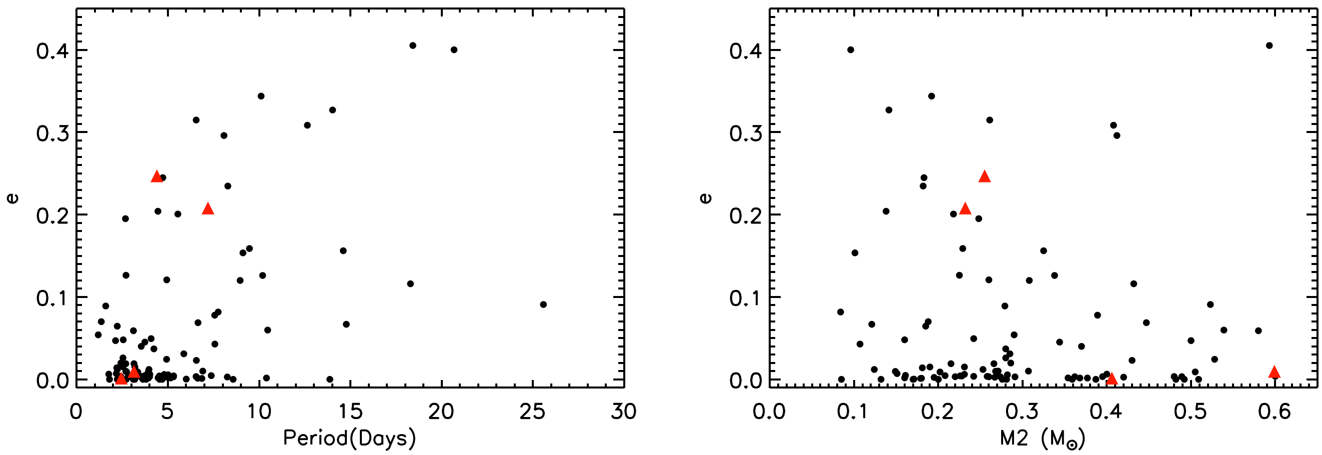


**Figure 6.** Left panel: scatter plot for eccentricity vs. period for the 97 F+M EBs compiled from the literature (black circles). Overplotted are the four EBs studied as a part of this work (red triangles). Right panel: scatter plot for eccentricity vs. companion mass ($M_2$) for the 97 F+M EBs compiled from the literature (black circles). Overplotted are the four EBs studied as a part of this work (red triangles). The literature sources are taken from Bouchy et al. (2005), Pont et al. (2005b), Pont et al. (2006), Beatty et al. (2007), Fernandez et al. (2009), Ofir et al. (2012), Tal-Or et al. (2013), Chaturvedi et al. (2014), Zhou et al. (2014), Eigmüller et al. (2016), von Boetticher et al. (2017), and Triaud et al. (2017).

abovementioned parameters needed in this equation from Table 3 and thereby estimate the synchronization timescale for SAO 106989 to be ∼2 Myr. Since the age of the star is more than this, we rightly see the orbital and rotational velocities for the star synchronized with each other. For HD 24465, we similarly estimate the synchronization timescale to be ∼28 Myr. Here too, the age of the star is more than the synchronization timescale, and we see the orbital and rotational velocities synchronized in this case as well. For EPIC 211682657, the synchronization timescale is very small, ∼0.03 Myr, due to its large mass ratio ($q$) and small period, and the same for HD 205403 EB is 0.2 Myr. These synchronization timescale values are similarly larger than the respective ages of the two EBs, and thereby we infer that all EBs are synchronized.

The circularization timescale as mentioned in Zahn (1977) is given in years as $t_{\rm circ} \sim (q(1+q)/2)^{-1}\ (a/R)^8 \sim 10^6 q^{-1}((1+q)/2)^{5/3} P^{16/3}$. For SAO 106989, this value is ∼5 Gyr. The same values for HD 24465, EPIC 211682657, and HD 205403 are ∼88, ∼0.67, and ∼0.2 Gyr, respectively. It is important to note that these estimations are based on the assumption that these stars have a convective envelope. Recently, Van Eylen et al. (2016) studied the orbital circularization rates of hot and cool stars from the *Kepler* EB catalog. The authors found that EBs having both components as hot–hot type (⩾6250 K) are more likely to have eccentric systems as compared to EBs having cool–cool (⩽6250 K) and a combination of hot–cool systems. This is mainly due to the tidal efficiency rate, which is dependent on the total mass and orbital period of the EB. Zahn (1977) derived a lower limit on $R_*/a$ (inverse of relative separation) as 0.025 for synchronization. Systems below this relative separation are found to be nonsynchronized. It is also important to note that these trends of $R_*/a$ and eccentricity are for solar age and composition. Orbits for systems having a lower limit of $R_*/a \sim 0.25$ are circular. Systems having a relative radius value smaller than 0.25 are eccentric in nature. Thus, we see that circularization is a much slower process than synchronization. From the current work, the $R_*/a$ for SAO 106989 is 0.11 and that for HD 24465 is 0.08. The relative radii for both these systems are larger than 0.025 but very small as compared to 0.25. Both the EBs have eccentricities greater than 0.2. Thus, we rightly conclude that the circularization timescales for these EBs are more than their ages. Though these EBs are synchronized for their rotational and orbital periods, they have not yet circularized. For the other two EBs, EPIC 211682657 and HD 205403, the $R_*/a$ is 0.21 and 0.19, respectively, which are relatively larger values than those for SAO 106989 and HD 24465. The $R_*/a$ values are sufficiently larger than the synchronization limit and comparable to the circularization limit. Moreover, the derived circularization timescales are comparable to the respective ages of the EBs. Thereby, we see these EBs are not only synchronized for their rotational and orbital periods but also have negligible eccentricities as compared to the other two EBs.

In order to analyze this argument carefully, we have compiled all the F+M systems characterized for their masses and orbital parameters from the literature. Out of the 97 F+M EBs, a major set of samples (75) comes from the recent paper Triaud et al. (2017), and the remaining 22 sources are from Bouchy et al. (2005), Pont et al. (2006), Beatty et al. (2007), Fernandez et al. (2009), Ofir et al. (2012), Tal-Or et al. (2013), Chaturvedi et al. (2014), Zhou et al. (2014), Eigmüller et al. (2016), and von Boetticher et al. (2017). In Figure 6, we have plotted eccentricity versus period for these 97 F+M EBs in the left panel and eccentricity versus secondary mass ($M_2$) in the right panel. The error bars (not shown in the scatter plots) on eccentricity and $M_2$ are, on average, between 2% and 5% of the actual values. We have overplotted the F+M EBs studied as part of this work on the eccentricity-versus-period and eccentricity-versus-$M_2$ plots as red triangles in Figure 6 in the left and right panels, respectively. As expected, we see that F+M EBs having short orbital periods are mostly circular, and the ones having longer periods show a range of eccentricities. The scatter seen in EB parameters can be attributed to different methods adopted for analysis. This is consistent with the tidal circularization theory by Zahn (1977). As seen from the right panel of the plot, less massive secondary companions have a range of eccentricities, and as the mass of the companion increases, the systems tend to show more circular orbits. The mass ratio, $q$, affects the tidal circularization rate. However, it is also important to note that the observed eccentricities are a function of the initial eccentricity at the time of system formation, and thereby the primordial eccentricity and circularization timescales would be larger (Mazeh 2008).

Two of the EBs studied here, SAO 106989 and HD 24465, follow the trends marginally with large eccentricities despite their short orbital periods. These EBs are thereby unique, as they belong to a category of a handful of such systems. EPIC 211682657 and HD 205403 are close to circular ($e \sim 0.009$ and $\sim 0.002$, respectively). The primaries for these two EBs are mid-F-type stars with higher rotational velocities. The tidal dissipation rates in such systems are expected to be less than those for the other two EBs. Short-period eccentric EBs have a higher probability of hosting a distant third body as a perturber (Mazeh 2008). Long-term monitoring of these targets will help discover any such trends, if present. Moreover, such systems are also prone to showing a wide range of obliquities for spin–orbit orientation as compared to stars with convective exteriors (Winn et al. 2010). Thus, a detailed investigation of SAO 106989 and HD 24465 on a longer timeline will be desirable in future.

### 4.2. Mass–radius Relation

We have inferred the radii of the program stars using photometry observations and the empirical Torres relation. A comparison for testing the isochrone-predicted M-dwarf parameters against the Torres relation is in order. We compared the derived radii of the low-mass companions in the EB systems based on our current work with Baraffe's grid of new models (Baraffe et al. 2015) that have updated molecular line lists, revised solar abundances, and line opacities for several important molecules. These updated models have been able to account for some of the flaws of the previous Baraffe models (Baraffe et al. 1998), such as predicting optical colors of the stars that are too blue (Baraffe et al. 2015). The masses of the M dwarfs, detected as companions to F-type stars discussed in this paper, range from 0.232 to 0.599 $M_{\odot}$.

The ages of all of the primary stars of the EBs are between 1 and 3 Gyr, as discussed in the previous section. From our RV analysis, we find that SAO 106989B has a mass of $0.256 \pm 0.005\, M_{\odot}$. With the Baraffe et al. (2015) models for 1 Gyr isochrones, the radius for $0.25\, M_{\odot}$ turns out to be $0.26\, R_{\odot}$ for [M/H] = 0.0. The value retrieved from the fitting of the KELT light curve is $R_B = 0.326 \pm 0.012\, R_{\odot}$. The similar estimate given by SW photometry is $R_B = 0.126\, R_{\odot}$. The noisy SW photometry data may have led to a diluted measurement of transit depth. Though the larger error bars cannot be ignored for the derived values, it is worth mentioning that the observationally derived radius for SAO 106989B is 20% larger than the theoretically derived values. From our current study, we have derived the mass of HD 24465B as $0.233 \pm 0.002\, M_{\odot}$. For [M/H] = 0.0, a $0.233\, M_{\odot}$ star has a radius of $0.23\, R_{\odot}$ (Baraffe et al. 2015). The value derived from *K2* photometry matches within the error bars of the predicted model. We have derived the mass of EPIC 211682657B as $0.599 \pm 0.017\, M_{\odot}$ based on the RV data from PARAS. We derive a radius of $0.566 \pm 0.005$ from *K2* photometry. The same value derived theoretically from the Baraffe et al. (2015) models is $\sim 0.557\, R_{\odot}$ for [M/H] = 0.0. The observed value matches the theoretically derived radius value. The mass derived for HD 205403B is $0.406 \pm 0.005\, M_{\odot}$ from our current RV data. The value for the radius derived from *STEREO* photometry is $0.444 \pm 0.014$. We derive the

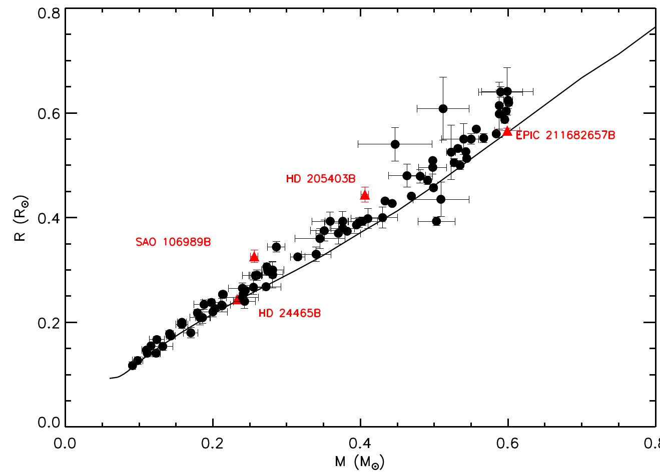


**Figure 7.** Mass–radius diagram for M dwarfs based on Baraffe models for 1 Gyr isochrone and solar metallicity. Overplotted in black circles are the M dwarfs taken from the literature as shown in Table 4, and the ones shown by red triangles are studied as a part of this paper. The masses and radii are plotted with their respective error bars.

theoretical value for the radius as $\sim 0.37\, R_{\odot}$ from the Baraffe et al. (2015) models, which is 17% less than the observed radius value.

Figure 7 plots a Baraffe isochrone for 1 Gyr and solar metallicity (Baraffe et al. 2015) in the mass–radius space (black solid line). Overplotted on this diagram are the observationally derived values for the four stars studied as a part of this work (red triangles). Also shown are the results taken from the literature for M dwarfs ($M \leqslant 0.6\, M_{\odot}$), which have masses and radii measured at best up to 10% (see Table 4 in Section 5 for the sources taken from the literature). From the figure, we see a disagreement between the observed radii of the stars and their theoretical predictions beyond $0.3\, M_{\odot}$. The M dwarfs below this mass limit seem to follow the theoretical M–R relation within the error bars. Above this mass limit, we see a huge scatter, which points toward a higher observationally derived radius value. Two of the stars as a part of this work follow a similar trend as that of the stars seen in the literature. The larger error bars on SAO 106989B are due to the relatively noisy KELT data set. The case is similar to that of HD 205403B, which has data from *STEREO* photometry. Both of these stars have radii 17%–20% larger than the theoretically predicted values. The remaining two stars, HD 24465B and EPIC 211682657B, have observed radii consistent with predictions from theory. The mass limit between stars that are fully convective and the ones that have radiative cores is $0.3\, M_{\odot}$. Convection is the most efficient mechanism of energy transport in the low-mass regime. The central density for the stars, which are fully convective (below $0.3\, M_{\odot}$), decreases with the hydrogen-burning phase. With reduced central densities, electron degeneracy effects dominate in the stellar interior, affecting thermal efficiency and further inhibiting flux transport. This inhibition leads to an increase in the stellar radii (Cassisi 2011). Strong magnetic fields inhibit convection, causing inflation of stellar radii (Mullan & MacDonald 2001; López-Morales & Ribas 2005). Single stars are known to be slow rotators, whereas many of the binaries are fast rotators depicting strong indications of X-ray activity from the corona and $H_{\alpha}$ activity from the chromosphere (Chabrier et al. 2007). Thus, the magnetic activity level for binaries can be 100 times more than for single stars (Mullan & MacDonald 2001).

**Table 4**
A Compilation of Known M Dwarfs ($M \leqslant 0.6\ M_{\odot}$) from the Literature Other for Masses and Radii Measured at Accuracies Better than or at Best Equal to 10

| Name of EB | Mass | Radius | Reference |
|---|---|---|---|
| J1219-39B | 0.091 ± 0.002 | 0.1174 ± 0.0071 | (1) |
| J2343+29[a] | 0.098 ± 0.007 | 0.127 ± 0.007 | (2) |
| HATS550-016B | 0.110 ± 0.006 | 0.147 ± 0.004 | (3) |
| NNSer-B | 0.111 ± 0.004 | 0.141 ± 0.002 | (4) |
| GKVir | 0.116 ± 0.003 | 0.155 ± 0.003 | (5) |
| GJ551 | 0.123 ± 0.006 | 0.141 ± 0.007 | (6) |
| HAT-TR-205 | 0.124 ± 0.010 | 0.167 ± 0.006 | (7) |
| HATS551-021B | 0.132 ± 0.014 | 0.154 ± 0.008 | (3) |
| KIC1571511B | 0.14136 ± 0.0051 | 0.17831 ± 0.0013 | (8) |
| WTS 19g4-020B | 0.143 ± 0.006 | 0.174 ± 0.006 | (9) |
| GJ699 | 0.158 ± 0.008 | 0.196 ± 0.008 | (6) |
| SDSS J1210+3347 | 0.158 ± 0.006 | 0.20 ± 0.003 | (10) |
| HATS551-019B | 0.17 ± 0.01 | 0.18 ± 0.01 | (3) |
| HATS551-027B | 0.179 ± 0.002 | 0.218 ± 0.007 | (11) |
| RRCaeB | 0.1825 ± 0.0139 | 0.209 ± 0.0143 | (12) |
| J0113+31B | 0.186 ± 0.010 | 0.209 ± 0.011 | (13) |
| 2MASS02405152+5245066 | 0.188 ± 0.014 | 0.234 ± 0.009 | (14) |
| T-Lyr1-01662 | 0.198 ± 0.012 | 0.238 ± 0.007 | (15) |
| HATS553-001B | 0.20 ± 0.02 | 0.22 ± 0.01 | (3) |
| KEPLER16B | 0.20255 ± 0.00066 | 0.22623 ± 0.00059 | (16) |
| AD2615B | 0.212 ± 0.012 | 0.233 ± 0.013 | (17) |
| KOI-126C | 0.2127 ± 0.0026 | 0.2318 ± 0.0013 | (18) |
| CMDraA | 0.2130 ± 0.0009 | 0.2534 ± 0.0019 | (19) |
| CMDraB | 0.2141 ± 0.0010 | 0.2534 ± 0.0019 | (19) |
| **HD 24465B**[a] | 0.233 ± 0.002 | 0.244 ± 0.001 | This work |
| T-Lyr0-08070B | 0.24 ± 0.019 | 0.265 ± 0.010 | (15) |
| SDSS-MEB-1B | 0.24 ± 0.022 | 0.248 ± 0.009 | (20) |
| KOI-126B | 0.2413 ± 0.0003 | 0.2543 ± 0.0014 | (18) |
| OGLE-TR-78B | 0.243 ± 0.015 | 0.240 ± 0.013 | (21) |
| HATS551-027A | 0.244 ± 0.003 | 0.261 ± 0.009 | (11) |
| AD2615A | 0.255 ± 0.013 | 0.267 ± 0.014 | (17) |
| **SAO 106989B**[a] | 0.256 ± 0.005 | 0.326 ± 0.012 | This work |
| 1RXSJ14727A | 0.2576 ± 0.0085 | 0.2895 ± 0.0068 | (22) |
| 1RXSJ14727B | 0.2585 ± 0.0080 | 0.2895 ± 0.0068 | (22) |
| NSV-S6550671B | 0.260 ± 0.02 | 0.290 ± 0.01 | (23) |
| SDSS-MEB-1A | 0.272 ± 0.02 | 0.268 ± 0.001 | (20) |
| SDSS J12120123 | 0.273 ± 0.002 | 0.306 ± 0.007 | (10) |
| LSPMJ1112B | 0.2745 ± 0.0012 | 0.2978 ± 0.005 | (24) |
| GJ3236B | 0.281 ± 0.015 | 0.3 ± 0.015 | (25) |
| GJ191 | 0.281 ± 0.014 | 0.291 ± 0.025 | (6) |
| HD 213597B[a] | 0.286 ± 0.012 | 0.344 ± 0.01 | (26) |
| T-Boo0-0080 | 0.315 ± 0.01 | 0.325 ± 0.005 | (15) |
| LP133-373A | 0.34 ± 0.02 | 0.330 ± 0.014 | (27) |
| LP133-373B | 0.34 ± 0.02 | 0.330 ± 0.014 | (27) |
| T-cyg-1-01385 | 0.345 ± 0.034 | 0.360 ± 0.019 | (15) |
| WTS 19e-3-08413B | 0.351 ± 0.019 | 0.375 ± 0.020 | (28) |
| OGLE-TR-6 | 0.359 ± 0.025 | 0.393 ± 0.018 | (29) |
| TAur0-13378 | 0.37 ± 0.03 | 0.37 ± 0.02 | (15) |
| GJ3236A | 0.376 ± 0.016 | 0.3795 ± 0.0084 | (25) |
| WTS 19c-3-01405B | 0.376 ± 0.024 | 0.393 ± 0.019 | (28) |
| MG1-2056316B | 0.382 ± 0.001 | 0.374 ± 0.002 | (30) |
| LSPMJ1112A | 0.3946 ± 0.0023 | 0.3860 ± 0.005 | (24) |
| CuCnCB | 0.3980 ± 0.0014 | 0.3908 ± 0.0094 | (31) |
| GJ411 | 0.403 ± 0.02 | 0.393 ± 0.008 | (6) |
| **HD 205403B**[a] | 0.406 ± 0.005 | 0.444 ± 0.014 | This work |
| WTS 19c-3-01405A | 0.410 ± 0.023 | 0.398 ± 0.019 | (28) |
| TCyg1-01385B | 0.43 ± 0.02 | 0.40 ± 0.02 | (15) |
| CuCnCA | 0.4333 ± 0.0017 | 0.4317 ± 0.0052 | (31) |
| MG1-646680B | 0.443 ± 0.002 | 0.427 ± 0.004 | (30) |
| KELTJ041621-620046A | 0.447 ± 0.05 | 0.540 ± 0.032 | (32) |
| WTS 19e-3-08413A | 0.463 ± 0.025 | 0.480 ± 0.022 | (28) |
| MG1-2056316A | 0.469 ± 0.002 | 0.441 ± 0.002 | (30) |
| WTS 19b-2-01387B | 0.481 ± 0.017 | 0.479 ± 0.013 | (28) |
| MG1-78457B | 0.491 ± 0.001 | 0.471 ± 0.008 | (30) |
| NSVS-01031772B | 0.498 ± 0.0025 | 0.509 ± 0.003 | (33) |

**Table 4**
(Continued)

| Name of EB | Mass | Radius | Reference |
|---|---|---|---|
| WTS 19b-2-01387A | 0.498 ± 0.019 | 0.496 ± 0.013 | (28) |
| MG1-646680A | 0.499 ± 0.002 | 0.457 ± 0.005 | (30) |
| GJ887 | 0.503 ± 0.025 | 0.393 ± 0.008 | (6) |
| OGLE-TR-34 | 0.509 ± 0.038 | 0.435 ± 0.033 | (29) |
| UNSW2AB | 0.512 ± 0.035 | 0.608 ± 0.06 | (34) |
| T-Lyr-17236B | 0.523 ± 0.006 | 0.525 ± 0.052 | (35) |
| MG1-78457A | 0.527 ± 0.002 | 0.505 ± 0.0075 | (30) |
| MG1-116309B | 0.532 ± 0.002 | 0.532 ± 0.006 | (30) |
| MG1-1819499B | 0.535 ± 0.001 | 0.5 ± 0.0085 | (30) |
| HIP96515AaB | 0.54 ± 0.03 | 0.55 ± 0.03 | (36) |
| NSVS-01031772A | 0.5428 ± 0.0027 | 0.526 ± 0.0028 | (33) |
| MG1-506664B | 0.544 ± 0.002 | 0.513 ± 0.0055 | (30) |
| NSVS-6550671A | 0.550 ± 0.01 | 0.550 ± 0.01 | (23) |
| MG1-1819499A | 0.557 ± 0.001 | 0.569 ± 0.0022 | (6) |
| MG1-116309A | 0.567 ± 0.002 | 0.552 ± 0.0085 | (30) |
| MG1-506664A | 0.584 ± 0.002 | 0.560 ± 0.0025 | (30) |
| BD-225866AaA | 0.5881 ± 0.0029 | 0.614 ± 0.045 | (37) |
| BD-225866AaB | 0.5881 ± 0.0029 | 0.598 ± 0.045 | (37) |
| HIP96515AaA | 0.59 ± 0.03 | 0.64 ± 0.01 | (36) |
| V530OriB | 0.5955 ± 0.0022 | 0.5873 ± 0.0067 | (38) |
| YYGemB | 0.5975 ± 0.0047 | 0.6036 ± 0.0057 | (39) |
| **EPIC 211682657B**[a] | 0.599 ± 0.017 | 0.566 ± 0.005 | This work |
| UNSW2AA | 0.599 ± 0.035 | 0.641 ± 0.045 | (34) |
| GuBooB | 0.600 ± 0.006 | 0.624 ± 0.016 | (40) |
| YYGemA | 0.6009 ± 0.0047 | 0.6196 ± 0.0057 | (39) |

**Note.** The M dwarfs studied in this paper are indicated in bold.
[a] PARAS spectra.

**References:** (1) Triaud et al. (2013); (2) Chaturvedi et al. (2016); (3) Zhou et al. (2014); (4) Parsons et al. (2010); (5) Parsons et al. (2012); (6) Ségransan et al. (2003); (7) Beatty et al. (2007); (8) Ofir et al. (2012); (9) Nefs et al. (2013); (10) Pyrzas et al. (2012); (11) Zhou et al. (2015); (12) Maxted et al. (2007); (13) Gómez Maqueo Chew et al. (2014); (14) Eigmüller et al. (2016); (15) Fernandez et al. (2009); (16) Doyle et al. (2011); (17) Gillen et al. (2017); (18) Carter et al. (2011); (19) Morales et al. (2009); (20) Blake et al. (2008); (21) Pont et al. (2005a); (22) Hartman et al. (2011); (23) Dimitrov & Kjurkchieva (2010); (24) Irwin et al. (2011); (25) Irwin et al. (2009); (26) Chaturvedi et al. (2014); (27) Vaccaro et al. (2007); (28) Birkby et al. (2012); (29) Bouchy et al. (2005); (30) Kraus et al. (2011); (31) Ribas (2003); (32) Lubin et al. (2017); (33) Lopez-Morales et al. (2006); (34) Young et al. (2006); (35) Devor et al. (2008); (36) Huélamo et al. (2009); (37) Shkolnik et al. (2010); (38) Torres et al. (2014); (39) Torres & Ribas (2002); (40) López-Morales & Ribas (2005).

Another possible scenario causing a mismatch in the observationally computed and theoretically derived radius are star spots seen as dark regions on the observable photosphere of the star due to the presence of local magnetic fields that suppress the convective motion and thereby energy transport from the stellar interior to the surface (Strassmeier 2009). Chabrier et al. (2007) concluded in their study that the inhibition of convection in fast-rotating stars and the presence of star spots on the stellar disk could affect the stellar models. Cool star spots are also reflective of the inhibition of energy by convective transport in the interior of the star. There is a possibility that the scatter in observational radii could be due to the large range of metallicities and stellar activity of the samples (López-Morales 2007). Berger et al. (2006) found in their study that the disagreement is larger among metal-rich stars than metal-poor stars. They concluded that current atmospheric models have missed some opacity components that may lead to larger radii for stars having higher metallicity. If we consider stars having the same mass, a decrease in stellar metallicity leads to a decrease in opacity. This, in turn, causes raised electron degeneracy, leading to inflated stellar radii (Cassisi 2011). An improper modeling of the molecular absorption coefficients due to incorrect abundance analysis results in an erroneous M–R relationship (Berger et al. 2006). López-Morales (2007) showed that stars with $[Fe/H] > -0.25$ show larger deviations in the radius measurements from the models than stars with $[Fe/H] < -0.25$. However, this issue needs to be further investigated. Therefore, it becomes imperative to detect and study more such systems and determine their masses and radii to very high precision.

Future spectroscopic observations and detailed photometry for all of these stars during their respective transits may enable us to observe the Rossiter–McLaughlin (RM) effect (Gaudi & Winn 2007) and help determine whether the secondary star is in retrograde or prograde orbital motion with respect to the rotation of the primary. This may lead to a better understanding of the binary formation mechanisms at a primordial stage. The M dwarfs peak more in the near-infrared, and we expect the spectra of the secondary to be seen with a larger telescope, as is the case of $SB_2$ systems. Since the companions are M dwarfs, future high-resolution near-infrared observations with instruments sensitive in the infrared wavelength region, like the upcoming HPF (Mahadevan et al. 2014) and CARMENES (Quirrenbach et al. 2010), will be able to provide accurate masses and radii of the companion M dwarfs.

## 5. Summary

We have detected and characterized four F+M EBs, SAO 106989, HD 24465, EPIC 211682657, and HD 205403, in short orbital periods from SW, *STEREO*, and *K2* EB candidate databases using RV data from PARAS and light-curve data from the respective photometry archives for the stars. The prominent results are summarized below.

1. Masses for the companion M dwarfs are determined as $0.256 \pm 0.005$, $0.233 \pm 0.002$, $0.599 \pm 0.017$, and $0.406 \pm 0.005\, M_{\odot}$, respectively.
2. The radii for the M-dwarf companions are found to be $0.326 \pm 0.012$, $0.244 \pm 0.001$, $0.566 \pm 0.005$, and $0.444 \pm 0.014\, R_{\odot}$, respectively. Since the error bars on the radius measurements for SAO 106989 and HD 205403 are relatively larger, precision photometry measurements in future are desirable.
3. One of these M dwarfs, HD 24465, with a mass less than $0.3\, M_{\odot}$, is found to have a radius that is in good agreement with the theoretical predictions, whereas the other one observed with KELT, SAO 106989, shows discrepancies mostly attributed to noisy data. The radius for the EB HD 205403 having a mass greater than $0.3\, M_{\odot}$ has a 17% higher value than the theoretically derived ones, whereas the case of EPIC 211682657 is consistent with theory. Stars less massive than $0.3\, M_{\odot}$ have totally convective interiors and are thus believed to follow the theoretical M–R relation.
4. We have estimated the rotational and orbital velocities for these EBs and found them to be synchronized, as expected theoretically. Out of the four EBs, SAO 106989 and HD 24465 show significant eccentricities, whereas EBs EPIC 211682657 and HD 205403 have smaller eccentricities.

Future long-term follow-up for these systems is essential. Similar studies of EBs in the near future will help clarify observational biases associated with the stellar evolutionary models.

The PARAS spectrograph is fully funded and being supported by the Physical Research Laboratory (PRL), which is part of the Department of Space, Government of India. The authors would like to thank the director of the PRL for his support. The data pipeline development was done in collaboration with Suvrath Mahadevan and Arpita Roy at Pennsylvania University, USA. We acknowledge Vaibhav Dixit, Vishal Shah, Arvind Rajpurohit, and the Mount Abu Observatory staff for their support during observations. This research has made use of the ADS and CDS databases, operated at the CDS, Strasbourg, France.

*Software:* PARAS PIPELINE (Chakraborty et al. 2014), PARAS SPEC (Chaturvedi et al. 2016), ISOCHRONES (Morton 2015), IRAF (Tody 1986, 1993), REDUCE (Piskunov & Valenti 2002), PHOEBE (Prša & Zwitter 2005; Prša et al. 2016), SPECTRUM (Gray 1999).

## ORCID iDs

Priyanka Chaturvedi https://orcid.org/0000-0002-1887-1192
Rishikesh Sharma https://orcid.org/0000-0001-8983-5300
Abhijit Chakraborty https://orcid.org/0000-0002-3815-8407

## References

Andersen, J. 1991, A&ARv, 3, 91
Baraffe, I., Chabrier, G., Allard, F., & Hauschildt, P. H. 1998, A&A, 337, 403
Baraffe, I., Homeier, D., Allard, F., & Chabrier, G. 2015, A&A, 577, A42
Baranne, A., Queloz, D., Mayor, M., et al. 1996, A&AS, 119, 373
Bardalez Gagliuffi, D. C., Gelino, C. R., & Burgasser, A. J. 2015, AJ, 150, 163
Barros, S. C. C., Demangeon, O., & Deleuil, M. 2016, A&A, 594, A100
Beatty, T. G., Fernández, J. M., Latham, D. W., et al. 2007, ApJ, 663, 573
Berger, D. H., Gies, D. R., McAlister, H. A., et al. 2006, ApJ, 644, 475
Birkby, J., Nefs, B., Hodgkin, S., et al. 2012, MNRAS, 426, 1507
Blake, C. H., Torres, G., Bloom, J. S., & Gaudi, B. S. 2008, ApJ, 684, 635
Blanco-Cuaresma, S., Soubiran, C., Heiter, U., & Jofré, P. 2014, A&A, 569, A111
Borucki, W., Koch, D., Batalha, N., et al. 2009, in IAU Symp. 253, Transiting Planets, ed. F. Pont, D. Sasselov, & M. J. Holman (Cambridge: Cambridge Univ. Press), 289
Bouchy, F., Bonomo, A. S., Santerne, A., et al. 2011a, A&A, 533, A83
Bouchy, F., Deleuil, M., Guillot, T., et al. 2011b, A&A, 525, A68
Bouchy, F., Pont, F., Melo, C., et al. 2005, A&A, 431, 1105
Brown, T. M., Latham, D. W., Everett, M. E., & Esquerdo, G. A. 2011, AJ, 142, 112
Carter, J. A., Fabrycky, D. C., Ragozzine, D., et al. 2011, Sci, 331, 562
Cassisi, S. 2011, arXiv:1111.6464
Chabrier, G. 2003, PASP, 115, 763
Chabrier, G., & Baraffe, I. 2000, ARA&A, 38, 337
Chabrier, G., Gallardo, J., & Baraffe, I. 2007, A&A, 472, L17
Chakraborty, A., Mahadevan, S., Roy, A., et al. 2014, PASP, 126, 133
Chaturvedi, P., Chakraborty, A., Anandarao, B. G., Roy, A., & Mahadevan, S. 2016, MNRAS, 462, 554
Chaturvedi, P., Deshpande, R., Dixit, V., et al. 2014, MNRAS, 442, 3737
Christian, D. J., Pollacco, D. L., Skillen, I., et al. 2006, MNRAS, 372, 1117
Claret, A., Gimenez, A., & Cunha, N. C. S. 1995, A&A, 299, 724
Clarkson, W. I., Enoch, B., Haswell, C. A., et al. 2007, MNRAS, 381, 851
Devor, J., Charbonneau, D., Torres, G., et al. 2008, ApJ, 687, 1253
Dimitrov, D. P., & Kjurkchieva, D. P. 2010, MNRAS, 406, 2559
Dotter, A., Chaboyer, B., Jevremović, D., et al. 2008, ApJS, 178, 89
Doyle, L. R., Carter, J. A., Fabrycky, D. C., et al. 2011, Sci, 333, 1602
Duquennoy, A., & Mayor, M. 1991, A&A, 248, 485
Eigmüller, P., Eislöffel, J., Csizmadia, S., et al. 2016, AJ, 151, 84
Emerson, J. P. 2001, in ASP Conf. Ser. 232, The New Era of Wide Field Astronomy, ed. R. Clowes, A. Adamson, & G. Bromage (San Francisco, CA: ASP), 339
Fernandez, J. M., Latham, D. W., Torres, G., et al. 2009, ApJ, 701, 764
Fuhrmann, K., & Chini, R. 2015, ApJ, 809, 107
Fuhrmann, K., Chini, R., Hoffmeister, V. H., & Bernkopf, J. 2012, MNRAS, 420, 1423
Gagné, J., Lafrenière, D., Doyon, R., Malo, L., & Artigau, É 2014, ApJ, 783, 121
Gaudi, B. S., & Winn, J. N. 2007, ApJ, 655, 550
Gillen, E., Hillenbrand, L. A., David, T. J., et al. 2017, arXiv:1706.03084
Gillon, M., Triaud, A. H. M. J., Demory, B.-O., et al. 2017, Natur, 542, 456
Gomez Maqueo Chew, Y. 2010, PhD thesis, Vanderbilt Univ.
Gómez Maqueo Chew, Y., Morales, J. C., Faedi, F., et al. 2014, A&A, 572, A50
Gray, R. O. 1999, SPECTRUM: A stellar spectral synthesis program, Astrophysics Source Code Library, ascl:9910.002
Gunn, J. E., Carr, M., Rockosi, C., et al. 1998, AJ, 116, 3040
Hartman, J. D., Bakos, G. Á., Noyes, R. W., et al. 2011, AJ, 141, 166
Hatzes, A. P., & Cochran, W. D. 1992, in European Southern Observatory Conf. and Workshop Proc. 40, ed. M.-H. Ulrich (Garching: ESO), 275
Henry, T. J., Jao, W.-C., Subasavage, J. P., et al. 2006, AJ, 132, 2360
Herrero, E., Morales, J. C., Ribas, I., & Naves, R. 2011, A&A, 526, L10
Huélamo, N., Vaz, L. P. R., Torres, C. A. O., et al. 2009, A&A, 503, 873
Hut, P. 1981, A&A, 99, 126
Irwin, J., Charbonneau, D., Berta, Z. K., et al. 2009, ApJ, 701, 1436
Irwin, J. M., Quinn, S. N., Berta, Z. K., et al. 2011, ApJ, 742, 123
Kallrath, J., & Milone, E. F. 2009, Eclipsing Binary Stars: Modeling and Analysis (New York: Springer)
Kane, S. R., Clarkson, W. I., West, R. G., et al. 2008, MNRAS, 384, 1097
Koch, D., Borucki, W., Basri, G., et al. 2007, in IAU Symp. 240, Binary Stars as Critical Tools & Tests in Contemporary Astrophysics, ed. W. I. Hartkopf, P. Harmanec, & E. F. Guinan (Cambridge: Cambridge Univ. Press), 236
Kraus, A. L., Tucker, R. A., Thompson, M. I., Craine, E. R., & Hillenbrand, L. A. 2011, ApJ, 728, 48
Kroupa, P. 2002, Sci, 295, 82
Kurucz, R. 1993, ATLAS9 Stellar Atmosphere Programs and 2 km/s grid. Kurucz CD-ROM No. 13 (Cambridge, MA: Smithsonian Astrophysical Observatory)

Lada, C. J. 2006, ApJL, 640, L63
Lister, T. A., West, R. G., Wilson, D. M., et al. 2007, MNRAS, 379, 647
López-Morales, M. 2007, ApJ, 660, 732
Lopez-Morales, M., Orosz, J. A., Shaw, J. S., et al. 2006, arXiv:astro-ph/0610225
López-Morales, M., & Ribas, I. 2005, ApJ, 631, 1120
Lubin, J. B., Rodriguez, J. E., Zhou, G., et al. 2017, ApJ, 844, 134
Luhman, K. L. 2000, ApJ, 544, 1044
Luhman, K. L., Loutrel, N. P., McCurdy, N. S., et al. 2012, ApJ, 760, 152
Luhman, K. L., Rieke, G. H., Young, E. T., et al. 2000, ApJ, 540, 1016
Mahadevan, S., Ramsey, L. W., Terrien, R., et al. 2014, Proc. SPIE, 9147, 91471G
Mathis, S., & Le Poncin-Lafitte, C. 2009, A&A, 497, 889
Maxted, P. F. L., O'Donoghue, D., Morales-Rueda, L., Napiwotzki, R., & Smalley, B. 2007, MNRAS, 376, 919
Mazeh, T. 2008, in EAS Publications Ser. 29, ed. M.-J. Goupil & J.-P. Zahn (Les Ulis: EDP Sciences), 1
Meibom, S., Barnes, S. A., Platais, I., et al. 2015, Natur, 517, 589
Meibom, S., Mathieu, R. D., & Stassun, K. G. 2006, ApJ, 653, 621
Moe, M., & Di Stefano, R. 2015, ApJ, 801, 113
Morales, J. C., Ribas, I., Jordi, C., et al. 2009, ApJ, 691, 1400
Morton, T. D. 2015, isochrones: Stellar model grid package, Astrophysics Source Code Library, ascl:1503.010
Mullan, D. J., & MacDonald, J. 2001, ApJ, 559, 353
Nefs, S. V., Birkby, J. L., Snellen, I. A. G., et al. 2013, MNRAS, 431, 3240
Neves, V., Santos, N. C., Sousa, S. G., Correia, A. C. M., & Israelian, G. 2009, A&A, 497, 563
Nordström, B., Mayor, M., Andersen, J., et al. 2004, A&A, 418, 989
Ofir, A., Gandolfi, D., Buchhave, L., et al. 2012, MNRAS, 423, L1
Ogilvie, G. I. 2014, ARA&A, 52, 171
Parsons, S. G., Gänsicke, B. T., Marsh, T. R., et al. 2012, MNRAS, 426, 1950
Parsons, S. G., Marsh, T. R., Copperwheat, C. M., et al. 2010, MNRAS, 402, 2591
Pecaut, M. J., & Mamajek, E. E. 2013, ApJS, 208, 9
Pepper, J., Pogge, R. W., DePoy, D. L., et al. 2007, PASP, 119, 923
Pilbratt, G. L., Riedinger, J. R., Passvogel, T., et al. 2010, A&A, 518, L1
Piskunov, N. E., & Valenti, J. A. 2002, A&A, 385, 1095
Pont, F., Bouchy, F., Melo, C., et al. 2005a, A&A, 438, 1123
Pont, F., Melo, C. H. F., Bouchy, F., et al. 2005b, A&A, 433, L21
Pont, F., Moutou, C., Bouchy, F., et al. 2006, A&A, 447, 1035
Poppenhaeger, K. 2017, in IAU Symp. 328, Living Around Active Stars, ed. D. Nandy, A. Valio, & P. Petit (Cambridge: Cambridge Univ. Press), 308
Prša, A., Conroy, K. E., Horvat, M., et al. 2016, ApJS, 227, 29
Prša, A., & Zwitter, T. 2005, ApJ, 628, 426
Pyrzas, S., Gänsicke, B. T., Brady, S., et al. 2012, MNRAS, 419, 817
Quirrenbach, A., Amado, P. J., Mandel, H., et al. 2010, Proc. SPIE, 7735, 773513
Ribas, I. 2003, A&A, 398, 239
Ribas, I., Morales, J. C., Jordi, C., et al. 2008, MmSAI, 79, 562
Salpeter, E. E. 1955, ApJ, 121, 161
Sangaralingam, V., & Stevens, I. R. 2011, MNRAS, 418, 1325
Ségransan, D., Kervella, P., Forveille, T., & Queloz, D. 2003, A&A, 397, L5
Shkolnik, E. L., Hebb, L., Liu, M. C., Reid, I. N., & Collier Cameron, A. 2010, ApJ, 716, 1522
Siverd, R. J., Beatty, T. G., Pepper, J., et al. 2012, ApJ, 761, 123
Skrutskie, M. F., Cutri, R. M., Stiening, R., et al. 2006, AJ, 131, 1163
Sousa, S. G., Santos, N. C., Adibekyan, V., et al. 2014, A&A, 561, A21
Strassmeier, K. G. 2009, A&ARv, 17, 251
Street, R. A., Christian, D. J., Clarkson, W. I., et al. 2007, MNRAS, 379, 816
Suárez, G., José Downes, J., Román-Zúñiga, C., et al. 2017, AJ, 154, 14
Tal-Or, L., Mazeh, T., Alonso, R., et al. 2013, A&A, 553, A30
Theissen, C. A., West, A. A., Shippee, G., Burgasser, A. J., & Schmidt, S. J. 2017, AJ, 153, 92
Tody, D. 1986, Proc. SPIE, 627, 733
Tody, D. 1993, in ASP Conf. Ser. 52, Astronomical Data Analysis Software and Systems II, ed. R. J. Hanisch, R. J. V. Brissenden, & J. Barnes (San Francisco, CA: ASP), 173
Torres, G. 2013, AN, 334, 4
Torres, G., Andersen, J., & Giménez, A. 2010, A&ARv, 18, 67
Torres, G., & Ribas, I. 2002, ApJ, 567, 1140
Torres, G., Sandberg Lacy, C. H., Pavlovski, K., et al. 2014, ApJ, 797, 31
Triaud, A. H. M. J., Hebb, L., Anderson, D. R., et al. 2013, A&A, 549, A18
Triaud, A. H. M. J., Martin, D. V., Ségransan, D., et al. 2017, A&A, 608, A129
Vaccaro, T. R., Rudkin, M., Kawka, A., et al. 2007, ApJ, 661, 1112
Vanderburg, A., & Johnson, J. A. 2014, PASP, 126, 948
Van Eylen, V., Winn, J. N., & Albrecht, S. 2016, ApJ, 824, 15
van Hamme, W. 1993, AJ, 106, 2096
von Boetticher, A., Triaud, A. H. M. J., Queloz, D., et al. 2017, A&A, 604, L6
Werner, M. W., Roellig, T. L., Low, F. J., et al. 2004, ApJS, 154, 1
Wilson, R. E., & Devinney, E. J. 1971, ApJ, 166, 605
Winn, J. N., Johnson, J. A., Howard, A. W., et al. 2010, ApJL, 723, L223
Wraight, K. T., Fossati, L., White, G. J., Norton, A. J., & Bewsher, D. 2012, MNRAS, 427, 2298
Wraight, K. T., White, G. J., Bewsher, D., & Norton, A. J. 2011, MNRAS, 416, 2477
Wright, E. L., Eisenhardt, P. R. M., Mainzer, A. K., et al. 2010, AJ, 140, 1868
York, D. G., Adelman, J., Anderson, J. E., Jr., et al. 2000, AJ, 120, 1579
Young, T. B., Hidas, M. G., Webb, J. K., et al. 2006, MNRAS, 370, 1529
Zahn, J.-P. 1977, A&A, 57, 383
Zahn, J.-P. 2008, in EAS Publications Ser. 29, ed. M.-J. Goupil & J.-P. Zahn (Les Ulis: EDP Sciences), 67
Zasche, P. 2016, OEJV, 176, 10
Zhou, G., Bayliss, D., Hartman, J. D., et al. 2014, MNRAS, 437, 2831
Zhou, G., Bayliss, D., Hartman, J. D., et al. 2015, MNRAS, 451, 2263